# Headland Rip Very Low Frequency Fluctuations and Surfzone Eddies During High-Energy Wave Events⌀

ARTHUR MOURAGUES,[a] KÉVIN MARTINS,[a] PHILIPPE BONNETON,[a] AND BRUNO CASTELLE[a]

[a] CNRS, UMR 5805 EPOC, University of Bordeaux, Pessac, France

ABSTRACT: A wave-group-resolving model is used to investigate the driving mechanisms and the spatiotemporal variability of very low frequency (VLF) fluctuations of a headland deflection rip, measured during a 4-m oblique wave event. Surfzone eddies (SZE) occurring in the presence of a strongly sheared longshore current $V$ at a longshore-uniform beach are first modeled. The spectral signature and the variability of SZE are displayed and compared with the literature. The model is then used to explore the dynamics of vorticity in the surf zone and against a headland under energetic oblique wave conditions. The resulting weakly sheared $V$ is found to host large-scale SZE propagating toward the headland at a speed decreasing seaward. Vorticity animations and spectral diagrams indicate that VLF fluctuations of the deflection rip are driven by the deflection of the upstream SZE. In line with measurements, periods from 40 min to 1 h dominate the spectrum hundreds of meters from the headland at low tide. At high tide, vorticity spectra in the rip are much narrower than in the surf zone, suggesting that the headland enforces the merging of SZE. This mechanism is further analyzed using idealized simulations with varying headland lengths, aiming at extending traditional deflection patterns at the VLF scale. Finally, we discuss the existence of a continuum in SZE driving mechanisms, going from fully wave-group-driven to both wave-group- and shear-instability-driven SZE for weakly and strongly sheared $V$, respectively. This continuum suggests the importance of wave groups to produce SZE under energetic wave conditions.

KEYWORDS: Coastal flows; Currents; Oceanic waves

## 1. Introduction

Surfzone eddies (SZE) are two-dimensional horizontal vorticity motions typically associated with frequencies as low as a few millihertz, namely, within the very low frequency (VLF) band (e.g., MacMahan et al. 2004; Reniers et al. 2007). Besides broadly contributing to mixing and dispersion processes in the nearshore (e.g., Clark et al. 2010), SZE can also affect the spatiotemporal variability of longshore currents, thus impacting the transport of sediments and pollutants (Deigaard et al. 1995). Several SZE driving mechanisms have been proposed (e.g., Bowen and Holman 1989; Long and Özkan-Haller 2009; Feddersen 2014). The first one that was put forward is associated with the presence of shear waves.

Shear waves are alongshore progressive vortical structures propagating in the surf zone with periods and alongshore wavelengths of $O(100)$ s and $O(100)$ m, respectively. These motions are commonly observed in the presence of a relatively strong mean (time-averaged) longshore current $[O(1)$ m s$^{-1}$; e.g., Oltman-Shay et al. 1989; Dodd et al. 1992] and result from instabilities due to cross-shore shear of the longshore current (Bowen and Holman 1989). They appear in the form of a meandering longshore current depicted by SZE with rather large velocity fluctuations. Observed root-mean-squared velocity

amplitudes of such SZE can reach half of the mean longshore current magnitude (Oltman-Shay et al. 1989; Lippmann et al. 1999; Noyes et al. 2004). These highly energetic motions can therefore span the entire surf zone, altering the nearshore circulation and, in particular, the cross-shore distribution of the longshore current. The presence of shear-instability-driven SZE can lead to a substantial cross-shore mixing of momentum in the surf zone, resulting in a smoother longshore current profile (Özkan-Haller and Kirby 1999). Surfzone eddies can also be ejected seaward giving rise to spatially and temporally transient rip currents (Özkan-Haller and Kirby 1999), representing a dangerous hazard for swimmers (Castelle et al. 2016).

Shear wave motions in the nearshore were first theoretically explained by Bowen and Holman (1989), who highlighted the importance of the seaward shear of the longshore current (cross-shore gradient of the longshore current magnitude) to characterize these instabilities. For a strongly sheared longshore current, the latter becomes unstable, disturbances (or unstable modes) with different wavelengths (wavenumber) are generated and propagate in the same direction of the longshore current at a speed proportional to the longshore current peak. This was confirmed by Oltman-Shay et al. (1989), who analyzed measurements collected at a longshore-uniform sandy beach under moderately energetic and highly oblique wave conditions (offshore significant wave height $H_s$ of 1.36 m and peak angle of wave incidence $\theta_p$ of 30°). Since the works of Bowen and Holman (1989) and Oltman-Shay et al. (1989), shear wave motions have been investigated in many studies which have been extensively reviewed in Dodd et al. (2000). The spectral signature of shear waves is very specific within the longshore wavenumber–frequency ($k$–$f$) spectrum. Most shear-wave-related energy is spread around a relatively linear

dispersion relation located outside of the region of surface gravity motions, indicating that, at a given cross-shore position, all unstable modes of these vorticity motions propagate at the same speed. By analyzing the cross-shore variability of shear waves, Noyes et al. (2004) suggested that the celerity of such motions is related to the local value of the mean longshore current. Subsequent two-dimensional horizontal (2DH) modeling studies have highlighted the mechanisms for shear wave energy dissipation through bottom friction and horizontal mixing (e.g., Dodd et al. 1992; Falqués and Iranzo 1994; Özkan-Haller and Kirby 1999). In particular, Özkan-Haller and Kirby (1999) used a phase-averaged model to depict complex vortex structures that result from shear instabilities. These structures are essentially made of energetic vorticity fronts and detaching eddies.

Including the effect of wave groups, Long and Özkan-Haller (2009) showed that the production of vorticity due to wave groups and shear instabilities can be of the same order. The inclusion of wave groups was shown to result in broader $k$–$f$ spectra and a more chaotic vorticity field. These authors also showed that the vorticity due to wave groups was dominant over shear instabilities for weakly oblique incident waves. Using a phase-resolving model, Feddersen (2014) showed that breaking wave vorticity forcing, which includes both breaking wave group and individual wave vorticity forcing, are the dominant vorticity generation mechanisms, compared to shear instabilities, except for highly oblique large waves. Overall, these results suggest that SZE are not necessarily always driven by shear instabilities but are driven by mechanisms that may change depending on the longshore current profile, which can substantially vary with incident wave conditions.

A significant number of measurement and modeling studies have investigated the spatiotemporal variability of surfzone eddies in the presence of a longshore current. However, most of these studies have been conducted for SZE propagating along longshore-uniform (barred or planar) sandy beaches under low- to moderate-energy wave conditions, with $H_s$ rarely exceeding 2 m. The eddy regime under energetic wave conditions is therefore poorly understood. For such conditions, the longshore current is generally wider, potentially resulting in a different seaward longshore current shear than under less energetic wave conditions. The cross-shore structure of the longshore current is yet known to play an important role in the shear wave regime such as their characteristic spatial and temporal scales and the range of unstable modes (e.g., Bowen and Holman 1989; Dodd and Thornton 1990; Baquerizo et al. 2001). Although never addressed, the variability of SZE and their driving mechanisms, under high-energy conditions can be potentially different than under low- to moderate-energy conditions. Last, there is a lack of knowledge on the behavior of SZE propagating along longshore nonuniform beaches (Dodd et al. 2000). In particular, the dynamics of SZE propagating over complex morphologies with geological constraints, such as bedrocks or headlands that are commonly present along rugged coastlines, is virtually unknown.

Along rugged or artificial coastlines, the presence of physical boundaries, such as natural headlands or man-made structures, can significantly disrupt the nearshore circulation. Under obliquely incident wave conditions, wave breaking induces a longshore current that can be deflected against boundaries (e.g., Scott et al. 2016), creating a so-called headland deflection rip (Castelle et al. 2016). This type of rip was measured during a 3-week field experiment conducted at La Petite Chambre d'Amour (PCA; Anglet, southwest France) beach in October 2018 (Mouragues et al. 2020b). The field site comprises complex morphological features such as bedrocks and a 500-m rocky headland (Saint Martin headland in Fig. 1g). During a 4-m oblique wave event, the longshore current was deflected seaward against the headland, resulting in a strong tidally modulated deflection rip extending hundreds of meters offshore (Figs. 1a,f). At low tide, energetic VLF fluctuations of the deflection rip were measured 800 m offshore, with dominant (most energetic) periods around 30 min and 1 h (see SIG1 in Fig. 1; Mouragues et al. 2020a). These fluctuations were successfully reproduced by Mouragues et al. (2021) using a wave-group-resolving 2DH model (XBeach SurfBeat mode, hereafter XB-SB; Roelvink et al. 2009) but their driving mechanisms and their spatiotemporal variability were not addressed. Following Mouragues et al. (2021), the present study uses XB-SB to investigate these fluctuations and their driving mechanisms.

The paper is organized as follows. Section 2 briefly presents the field site and the experimental setup. In section 3, the XB-SB model, its implementation, and its methods for analyzing rotational motions, which includes the computation of their $k$–$f$ spectra and their bulk characteristics, are described. In section 4, the model is used to simulate surfzone eddies in the presence of a longshore current measured during the SandyDuck experiment (Duck, North Carolina). This first modeling experiment ensures that the model is able to reproduce SZE at a longshore-uniform sandy beach under moderate wave conditions. Model performances are assessed by comparing bulk characteristics of eddies and their spatiotemporal variability with previous studies. The ability of the model to reproduce SZE observed during the SandyDuck setup suggests that it can be used to simulate such motions occurring over more complex morphology and under more energetic wave conditions and to further explore their variability. Hence, in section 5, we investigate surfzone eddies and headland rip VLF fluctuations at PCA under energetic wave conditions and for different tidal levels. For this investigation, 20-h-long model simulations with a constant tidal level are set up in order to simulate a significant number VLF fluctuations [with periods < $O(1)$ h] and to fix the cross-shore location of wave breaking, thus removing the tidal modulation of surfzone circulation which was strong in the measurement dataset (see Figs. 1a,f). These model setups therefore subsequently allow addressing, through statistically significant spectrum analysis and a stationary state of VLF surfzone currents, the correct exploration of such motions. The mean (time-averaged) circulation patterns and the presence of SZE at low tide and high tide are then emphasized. The last part of section 5 presents the spatiotemporal (frequency) variability of vorticity in the surf zone and along the headland, showing that VLF fluctuations measured and modeled off the headland tip are related with SZE propagating in the upstream longshore current. In section 6, the findings of this study are discussed. The discussion includes the control of morphology on VLF fluctuations,
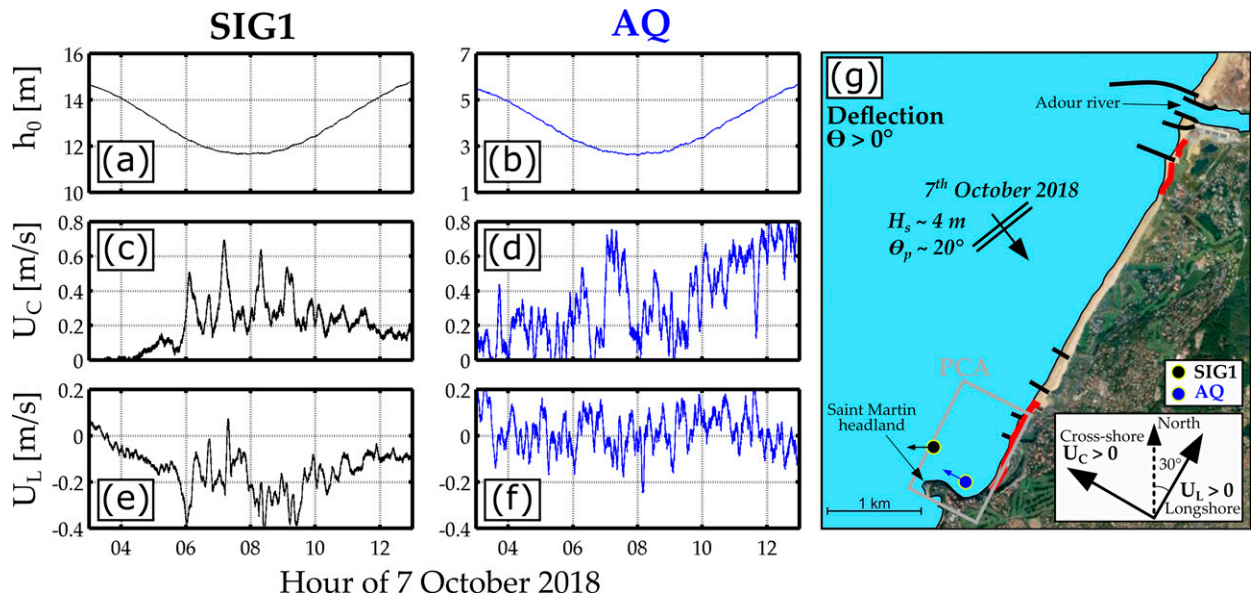
FIG. 1. (a),(b) Time series of water depth $h_0$; (c),(d) 5-min running-averaged cross-shore velocity $U_C$; and (e),(f) longshore velocity $U_L$ measured at two instrument locations (SIG1 and AQ, respectively) on 7 Oct 2018. (g) The location of the field site (PCA; gray rectangle), the two instrument locations (black and blue points), and the approximate direction of the measured current (black and blue arrows based at the points). The offshore significant wave height and peak angle of wave incidence ($H_s$ and $\theta_p$) are also indicated. Note that the bathymetry map and the entire array of instruments are shown in Fig. 2.

with suggestions for future research. The effect of wave group variability on surfzone rotational motions is also discussed, suggesting that wave group forcing may be the primary driver of VLF fluctuations of the rip during the high-energy wave event, rather than shear instabilities of the longshore current. Conclusions and perspectives for future works are finally drawn in section 7.

## 2. Field experiment

From 3 to 26 October 2018, a field experiment was conducted at La Petite Chambre d'Amour (PCA; Fig. 2a) beach located in Anglet in the south of the Aquitaine coast (southwest France). This rugged coast is a mesotidal high-energy environment that is regularly exposed to energetic Atlantic swells coming from the WNW direction (Abadie et al. 2005). PCA is a double-barred sandy beach located at the southern end of a 4-km embayment, comprising six groynes, bounded by the Adour River to the north and by the Saint Martin 500-m rocky headland to the south (Fig. 1g). The reader is referred to Mouragues et al. (2020a,b) for a detailed description of the field site and of the experiment.

A large array of instruments was deployed to measure and study the natural variability of wave-induced circulation at a high-energy geologically constrained beach. In particular, Acoustic doppler current profilers (ADCPs) were installed near the headland to collect high-frequency Eulerian velocity measurements (Fig. 2a). On 7 October 2018, obliquely incident energetic waves ($H_s \approx 4.0$ m and $\theta_p \approx 20°$) induced an intense deflection rip flowing against the headland. At low tide, high velocities were measured at the most offshore ADCP located

800 m offshore sitting at 12 m depth (Figs. 1, 2a). Time-averaged current velocities showed energetic VLF fluctuations with dominant periods of around 30 min and 1 h and associated peak velocities up to 0.7 m s$^{-1}$ (see, e.g., Figs. 1c,e). These fluctuations were numerically reproduced by Mouragues et al. (2021) using XB-SB, which model domain is shown in Fig. 2b. The analysis of modeling results further suggested that the rip actually extended up to 1600 m offshore and was strongly modulated by tides (see Figs. 1a,f; Mouragues et al. 2020a, 2021). The modeling approach used in the present study is similar to that of Mouragues et al. (2021) and is described in the following section.

## 3. Modeling surfzone vortical motions

### a. Modeling strategies

Over the past decades, several numerical modeling strategies have been employed in order to simulate surfzone eddies. These approaches mostly differ in terms of the wave scale resolved, ranging from phase-averaged models excluding wave groups (hereafter referred to as fully phase-averaged models; e.g., Özkan-Haller and Kirby 1999; Noyes et al. 2005) or including wave groups (hereafter referred to as wave-group-resolving models; e.g., Reniers et al. 2007; Long and Özkan-Haller 2009) to models simulating motions at the individual wave scale (Feddersen 2014). Fully phase-averaged models have been applied to assess, in particular, the effect of bottom friction and horizontal mixing on shear waves and their cross-shore variability. Because these models use a steady forcing to drive the nearshore circulation (i.e., averaged over many wave groups), they can only reproduce VLF scales ($f < 0.004$ Hz) associated
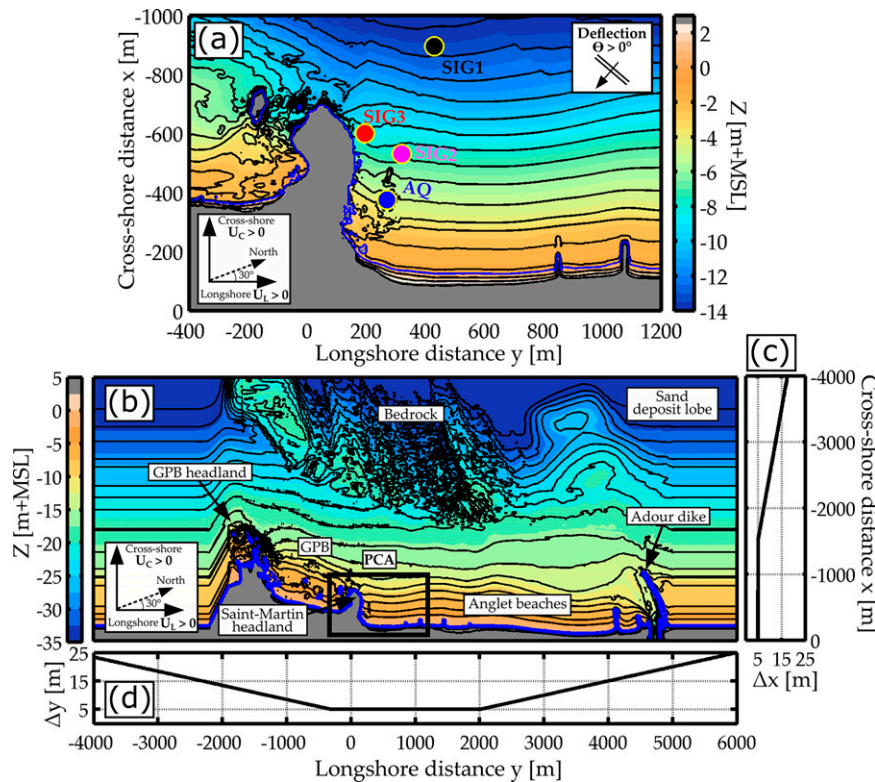
FIG. 2. (a) Bathymetry map of the field site (PCA; black lines show 1-m spaced elevation contours), whose location is shown by a black rectangle in (b) the full model domain (black lines show 2-m spaced elevation contours). Color indicates elevation relative to the mean sea level (m MSL), the blue line is the MSL contour, and colored points indicate the ADCP location. (c),(d) The cross-shore ($\Delta x$) and longshore ($\Delta y$) mesh step size, respectively.

with shear instabilities of the mean current, and not vorticity motions at the wave group scale. However, accounting for the variability of the wave forcing at scales at least similar to wave groups is essential for better reproducing surfzone rotational motions (Long and Özkan-Haller 2009; Feddersen 2014).

Feddersen (2014) used a Boussinesq model to simulate the dynamics of SZE that were measured during the SandyDuck experiment. Such a modeling approach allows the simulation of the vorticity field generated by shear instabilities and through wave breaking at both the individual and wave group scales. However, the submetric spatial resolution required to accurately reproduce motions at this scale still makes the use of these models computationally challenging over large spatial domains [$>O(10)$ km$^2$] and for long periods of time (temporal scale of a storm). In this context, wave-group-resolving models appear as a good compromise since they are much less costly than fully phase-resolving approaches while keeping the ability of these models to reproduce the vorticity generated by wave groups. Wave-group-resolving models such as XB-SB use a wave forcing varying at the wave group scale to drive the nearshore circulation, allowing to simulate low-frequency surf-zone motions which include infragravity and VLF motions. This approach has been used by several authors to reproduce the low-frequency variability of circulation along rip-channeled

open beaches (Reniers et al. 2006, 2007) and to simulate vorticity motions that result from obliquely incident wave groups along a longshore-uniform open beach (Long and Özkan-Haller 2009). The XB-SB wave-group-resolving approach has here been chosen to investigate the driving mechanism and the spatiotemporal variability of VLF fluctuations of the deflection rip at PCA. XBeach is a morpho-dynamic model initially developed to reproduce storm response of sandy beaches where infragravity swash is dominant (Roelvink et al. 2009). It solves the coupled 2DH equations for wave propagation, flow, sediment transport, and bottom changes [see Roelvink et al. (2009) for a model description]. The short-wave effects on currents are modeled through the radiation stress gradients approach (Longuet-Higgins and Stewart 1964). In this paper, sediment transport and bottom change modules are disabled as only hydrodynamics (longshore current and deflection rip) is investigated.

### b. Implementation of the XBeach model

Based on the input wave spectrum, the SurfBeat approach uses a random phase selection procedure to reconstruct time series of free surface elevation, from which the short-wave energy varying at the wave-group scale can be extracted and used to force the spectral wave model (see Roelvink et al. 2009, 2018). The circulation model is forced with elevations and currents corresponding
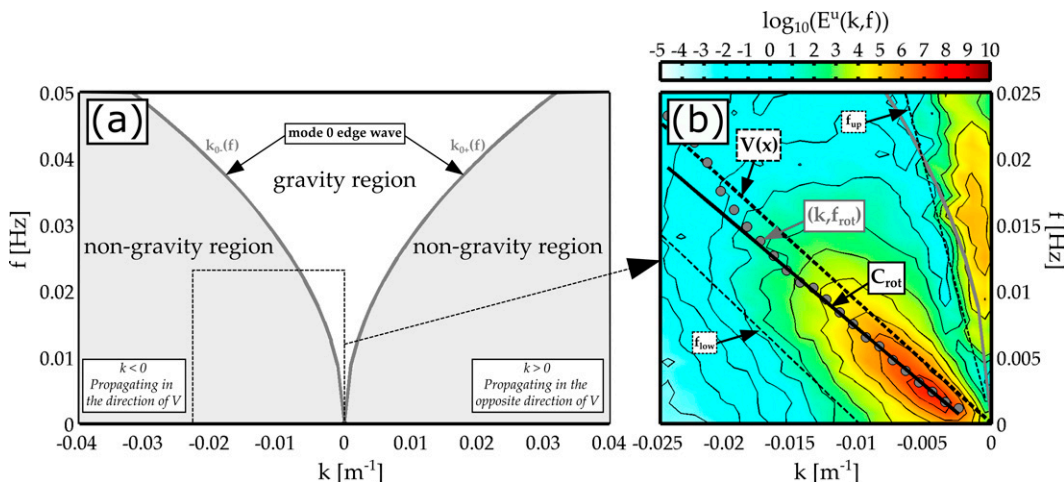
FIG. 3. (a) Schematic of a $k$–$f$ spectrum [$E(k, f)$] illustrating gravity and nongravity regions (after MacMahan et al. 2004). These regions are separated by the mode 0 edge wave [gray lines; computed with slope $\tan(\beta) = 0.03$]. (b) Zoom of a modeled $k$–$f$ spectrum of cross-shore velocities $E^u(k, f)$ showing eddies propagating in the direction of the longshore current. The solid gray line shows the mode 0 edge wave dispersion line. Thin dashed black lines indicate the upper and lower dispersion lines ($f_{up}$ and $f_{low}$, respectively) used to compute the rotational motion frequency $f_{rot}(k)$ (gray points). The black line shows the dispersion line resulting from the fitting of $k$–$f_{rot}$ and whose slope is the estimated eddy celerity $C_{rot}$. The thick dashed black line shows the dispersion line of the local longshore current magnitude $V(x)$.

to the incident bound infragravity waves computed from the generated time series of surface elevation following Herbers et al. (1994). The free surface elevation time series are generated using a random set of phases, but the model allows them to be saved so that the exact same boundary conditions can be used between numerical tests. This method will often be used in this paper to analyze the spatial–temporal variability of hydrodynamics (e.g., vorticity) between different model setup (e.g., morphological setup, free parameter calibration).

The XBeach model includes several free parameters requiring calibration with measurements. For the modeling experiments carried out in this paper, three free parameters were found to significantly impact the modeled hydrodynamics: the breaking parameter $\gamma$, a bed friction Chezy coefficient $C$, and a mixing free parameter $c_s$. The first two parameters are important, in particular, to the surfzone width and to the intensity of the longshore current, respectively. The third parameter alters the value of the eddy viscosity $\nu_h$ that controls the horizontal mixing. Increasing the eddy viscosity is known to have a damping effect on shear instabilities along with increasing their longshore length scales (e.g., Falqués and Iranzo 1994; Özkan-Haller and Kirby 1999). In XBeach, $\nu_h$ can be parameterized, using a Smagorinsky model, as a function of $c_s$, velocity spatial gradients and mesh step sizes:

$$\nu_h = c_s^2 2^{1/2} \sqrt{\left(\frac{\partial u}{\partial x}\right)^2 + \left(\frac{\partial v}{\partial y}\right)^2 + \frac{1}{2}\left(\frac{\partial u}{\partial x} + \frac{\partial v}{\partial y}\right)^2} \Delta x \Delta y, \qquad (1)$$

where $\Delta x$ and $\Delta y$ are the mesh step sizes.

Calibration of these three parameters was made by finding their values that minimize discrepancies between model outputs and measurements (running-averaged velocities or rotational

velocities). Model calibration results are described in sections 4 and 5 and are also indicated in Table A1 (see appendixes A and B). Finally, it should be noted that the effect of currents on waves was neglected.

### c. Vortical motion analysis

#### 1) WAVENUMBER–FREQUENCY SPECTRUM

To investigate surfzone eddy motions, wavenumber-frequency spectra ($k$–$f$, where $k$ is the longshore wavenumber in $m^{-1}$) of the cross-shore velocity $u$, the longshore velocity $v$, and of the associated vorticity $q = dv/dx - du/dy$ are computed. Along a longshore transect located at a given cross-shore position, modeled $u$, $v$ and $q$ are outputted every 10 s (sampling frequency $f_s = 0.1$ Hz) and every $\Delta y$ m (longshore mesh size; sampling longshore wavenumber $k_s = 1/\Delta y$) and stored into 2D matrices. A 2D fast Fourier transform is then applied to these matrices to estimate the energy density at each wavenumber and frequency $E(k, f)$. Wavenumber–frequency spectra of $u$, $v$, and $q$ are hereafter referred to as $E^u(k, f)$, $E^v(k, f)$, and $E^q(k, f)$, respectively.

Wavenumber–frequency spectra are typically partitioned into a gravity region and a nongravity region (see Fig. 3a), which are separated by the mode 0 edge wave dispersion line which is computed following Eckart (1951). The gravity region typically hosts gravity wave motions such as edge waves which can remain trapped within the surf zone and propagate down the coast or leaky waves which may exit the surf zone and propagate seaward. On the other hand, the nongravity region may host energetic rotational motions such as shear waves. Figure 3b shows a typical $E(k, f)$ that is computed in this study and highlights the presence of vorticity motions propagating in the direction of the mean longshore current $V$ ($k < 0$). The spectral signature of these motions resembles the spectral signature of shear waves

consisting of a near-linear dispersion line and for which a representative eddy celerity can be estimated (e.g., Oltman-Shay et al. 1989; Özkan-Haller and Kirby 1999; Noyes et al. 2004).

### 2) EDDY CELERITY

A representative eddy celerity $C_{rot}$ can be estimated as the $E(k, f)$ ridge slope. To estimate $C_{rot}$, a method similar to Özkan-Haller and Kirby (1999) is employed. For each wavenumber, a rotational motion frequency $f_{rot}(k)$ is computed by integrating $E(k, f)$ over a rotational motion frequency region:

$$f_{rot}(k) = \frac{\int_{f_{low}}^{f_{up}} f E(k,f)df}{\int_{f_{low}}^{f_{up}} E(k,f)df}, \tag{2}$$

where $f_{up}$ and $f_{low}$ are the upper and lower cutoff frequency lines delimiting the $k$–$f$ region attributed to surfzone eddies (dashed thin black lines in Fig. 3b). These cutoff lines were set to $f_{up} = 4V(x)k$ and $f_{low} = V(x)(k + 0.01)$, with $V(x)$ being the value of the mean longshore current (dashed thick black line in Fig. 3b) at the cross-shore position $x$, where the longshore transect is located. This method leads to the points $k$–$f_{rot}$ (gray points in Fig. 3b) that are used to fit a straight dispersion line whose slope corresponds to the estimated $C_{rot}$ (plain thick black line in Fig. 3b). For the fitting procedure, each data point $k$–$f_{rot}$ is weighted by the total energy $\int_{f_{low}}^{f_{up}} E(k,f)df$. It should be noted that, as its name suggests, $C_{rot}$ is a celerity representative of the most energetic rotational motions. As shown by the following results, interactions between eddies may occur which tends to increase discrepancies between the individual eddy celerity and $C_{rot}$. Note that the spectral signature of such eddy interactions is emphasized by the relative broadness of the $k$–$f$ spectrum (see, e.g., Fig. 3b)

### 3) ROTATIONAL VELOCITIES

The total frequency spectrum $E(f)$ is computed by integrating $E(k, f)$ over all wavenumber as

$$E(f) = \int_{-k_N}^{+k_N} E(k,f)dk, \tag{3}$$

where $k_N = k_s/2$ is the Nyquist wavenumber. The spectrum of rotational motions $E_{rot}(f)$ is calculated by integrating $E(k, f)$ over regions outside the mode 0 edge wave dispersion line $[k_{0-}(f)$ and $k_{0+}(f)$; see Fig. 3a]:

$$E_{rot}(f) = E(f) - E_{gw}(f), \tag{4}$$

where the spectrum of irrotational motions $E_{gw}(f)$ is given by

$$E_{gw}(f) = \int_{k_{0-}(f)}^{k_{0+}(f)} E(k,f)dk. \tag{5}$$

The total, cross- and longshore root-mean-square rotational velocities ($U_{rms,rot}$, $u_{rms,rot}$, and $v_{rms,rot}$, respectively) are then computed as

$$(U_{rms,rot})^2 = \int_{f_1}^{f_2} [E_{rot}^u(f) + E_{rot}^v(f)]df, \tag{6a}$$

$$(u_{rms,rot})^2 = \int_{f_1}^{f_2} E_{rot}^u(f)df, \tag{6b}$$

$$(v_{rms,rot})^2 = \int_{f_1}^{f_2} E_{rot}^v(f)df, \tag{6c}$$

where $f_1$ and $f_2$ are the lower and upper cutoff frequencies. It should be noted that these rotational velocities are velocities associated with rotational motions which include motions resulting from shear instabilities of the mean longshore current and from wave group forcing (when included).

## 4. Assessment of the model at a longshore-uniform sandy beach

In this section, the model ability to accurately simulate the dynamics of surfzone eddies propagating at a longshore-uniform sandy beach is investigated. This section serves as a model validation step for simulating SZE arising over a 2D barred beach under moderate energy wave conditions. In addition, a brief sensitivity analysis to different parameters is conducted, whose results are compared with previous studies.

The model is setup at the longshore-uniform barred sandy beach of Duck (North Carolina), for which many shear wave studies build on [see Dodd et al. (2000) for a shear wave study review]. The model is calibrated against measurements collected on 1 November 1997 as part of the SandyDuck experiment described in Noyes et al. (2004). This event was characterized by highly oblique and moderate-energy wave conditions, with offshore $H_s = 1.49$ m and mean wave angle $\theta = 21°$. The latter conditions produced a strong and narrow longshore current $V$, peaking around 0.9 m s$^{-1}$ (time-averaged) with a seaward width $\Delta$ (cross-shore distance between the peak position and the offshore near-zero current intensity) of around 150 m (Noyes et al. 2005; Feddersen 2014). This strongly sheared current (mean seaward shear $V_{max}/\Delta \approx 0.006$ s$^{-1}$) was unstable and hosted longshore-propagating surfzone eddies driven, at least partially, by shear instabilities (Noyes et al. 2005; Feddersen 2014).

In the following sections, XB-SB is first calibrated against measurements presented in Noyes et al. (2005). The calibrated model is then used to investigate the spatiotemporal variability of vorticity which is compared with previous studies. The computational domain extends 1000 and 1000 m in the cross-shore $x$ and longshore $y$ direction, respectively, with mesh resolution set to 2 m. The bathymetry is made of a longshore-uniform cross-shore depth profile that is representative of the instrumented transect, with the shoreline and a submerged inner sandbar located around $x = 110$ m and $x = 160$ m.

The model is forced by a Jonswap spectrum with the same bulk parameters as measurements ($H_s$, peak period $T_p$, $\theta$, and directional spreading $\sigma_\theta$) estimated at the 8-m depth pressure gauges array (Long 1996). Similar to Noyes et al. (2005), the period of simulation is set to 8 h with the last 4 h used for analysis. It should be noted that a sensitivity analysis to the
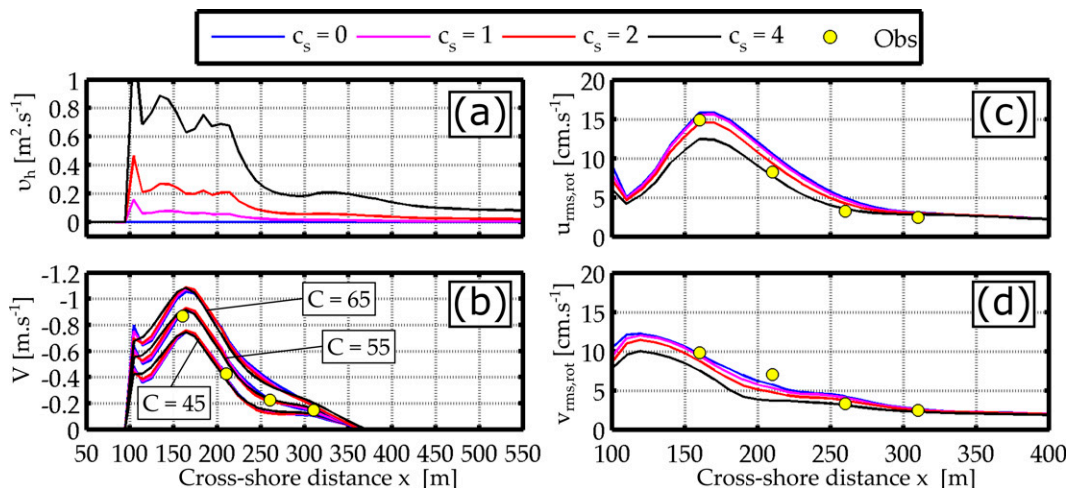
FIG. 4. Bottom friction ($C$) and horizontal mixing ($c_s$) coefficient sensitivity to the mean longshore current and to rotational motions (including shear waves). Cross-shore profile (a) of the horizontal viscosity $\nu_h$ (for $C = 55$ m$^{1/2}$ s$^{-1}$); (b) of the mean longshore current $V$; and (c),(d) of root-mean-square cross- and longshore rotational velocities $u_{\mathrm{rms,rot}}$ and $\nu_{\mathrm{rms,rot}}$, respectively (for $C = 55$ m$^{1/2}$ s$^{-1}$). Yellow points indicate observations from Noyes et al. (2005).

longshore domain length and mesh resolution was conducted and indicated that these parameters have a little impact on eddy bulk characteristics (not shown). Note that a mesh resolution of 1 and 2 m gave similar results while a mesh resolution of 5 m resulted in lower rotational velocities.

### a. Model calibration

Figure 4 displays the sensitivity of the time-averaged longshore current $V(x)$ (Fig. 4b) and rotational velocities (Figs. 4c,d) to bottom friction and horizontal mixing. Bottom friction Chezy coefficient $C = 55$ m$^{1/2}$ s$^{-1}$ best replicates the measured $V(x)$ while the eddy viscosity coefficient $c_s = 1$ correctly reproduces the spatial distribution of both cross-shore and longshore rotational velocities. Both these parameter values are taken for the following analysis (see Table A1). Of note, this eddy viscosity coefficient leads to a cross-shore profile of eddy viscosity (Fig. 4a) that is relatively similar to the ones shown in Özkan-Haller and Kirby (1999).

In line with previous studies (e.g., Özkan-Haller and Kirby 1999), increasing the horizontal mixing (increasing $c_s$) leads to less energetic rotational motion amplitudes. In addition, it should be noted that XB-SB is slightly better able at computing these amplitudes compared to the fully phase-averaged model used in Noyes et al. (2005). This is because including wave groups leads to a broader spectrum than when excluding wave groups (Long and Özkan-Haller 2009). The control of wave groups on the dynamics of rotational motions will be discussed in section 6. Last, it should be noted that a local bottom-slope-dependent wave dissipation coefficient (following Pezerat et al. 2021) was implemented and used for the Sandy-Duck modeling experiment. The latter implementation allows to prevent a substantial overdissipation of incident wave energy occurring seaward of the bar. Such a slope-dependent coefficient was not used for the Anglet modeling experiment as the

cross-shore distribution of the longshore current was not measured during the field experiment.

### b. Surfzone eddy variability

The calibrated model is now used to explore the spatiotemporal variability of vorticity. Figure 5 shows wavenumber–frequency spectra of vorticity $[E^q(k, f)]$ at four cross-shore positions seaward of the longshore current peak position. The spectra of modeled vorticity are in qualitative agreement with the spectra of observed velocities shown in Noyes et al. (2005), exhibiting, in particular, the presence of shear waves propagating in the direction of $V$. In line with previous studies, shear-wave-related energy and the range of energetic frequencies decrease seaward. The most energetic longshore length and period are order of 200 m and 200 s, respectively. Because both irrotational and rotational motions populate velocity spectra, shear wave motions are best detected using vorticity spectrum and will hereafter used to investigate rotational motions. An example of $u$, $v$, and $q$ spectra is provided in Fig. B1 to illustrate this point.

Although the eddy celerity estimated from velocities can be up to 20% higher than celerity estimated from vorticity, the entire set of estimated celerities are of the same order of magnitude and is proportional to the local value of the mean longshore current (see Fig. 6), which is in agreement with past studies (Noyes et al. 2004, 2005). Eddy celerities reach the longshore current peak at its peak position and decrease seaward. For each estimated celerity, its standard deviation computed for different eddy viscosity coefficients is indicated, showing that horizontal mixing does not strongly impact eddy celerities (with a maximum deviation of 6%), which is in line with the literature (Özkan-Haller and Kirby 1999).

The spatiotemporal variability of vorticity modeled at Duck is shown in Fig. 7. This figure displays snapshots and time–space diagram of the 100-s running averaged vorticity along a seaward
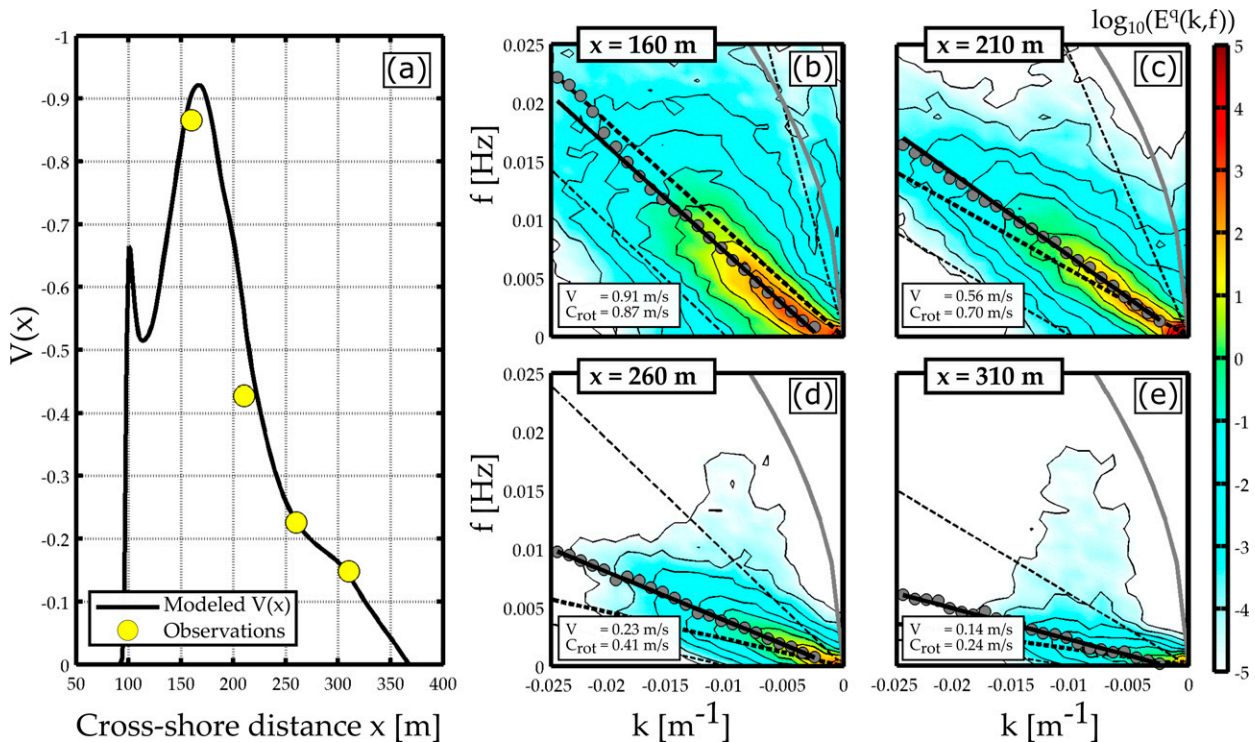
FIG. 5. (a) Cross-shore profile of the modeled mean longshore current $V(x)$. Yellow points indicate observations. (b)–(e) Modeled wavenumber–frequency spectra of vorticity $q$ $[E^q(k, f)]$ at the same cross-shore positions of observations ($x = 160, 210, 260$, and $310$ m). For each panel, the local value of the mean longshore current $V$ and the estimated eddy celerity $C_{rot}$ are indicated. The definition of multiple dispersion lines is the same as in Fig. 3b.

transect, emphasizing the presence of longshore-propagating vorticity fronts and detaching eddies. Snapshots indicate the presence of a vorticity front pair (positive and negative fronts) located near the longshore current peak position, propagating with the longshore current (right to left) and with longshore lengths of around 200 m. Some vorticity fronts may sometimes stretch until breaking down into two fronts with the main front continuing its course with the longshore current and the other secondary front being expelled offshore (detached eddy). Two successive fronts may also merge together which results in a larger front. It is suggested that such eddy interactions result in some discrepancies between the mean current and the estimated celerity seaward of the mean current peak position (see Fig. 6; Long and Özkan-Haller 2009). To better visualize vorticity fronts and their interactions, the reader is referred to the vorticity animation (see supplemental material). All these results are in good agreement with vorticity patterns previously modeled for similar setup (Özkan-Haller and Kirby 1999; Long and Özkan-Haller 2009).

The previous results indicate that XB-SB is able to simulate the dynamics of surfzone eddies at a longshore-uniform sandy beach under moderate energy wave conditions. The main characteristics (length and time scales, amplitudes) of SZE are well reproduced by the model. In the next sections, the model is used to investigate SZE and VLF fluctuations of a headland deflection rip occurring at a geologically constrained beach and under high-energy wave conditions.

## 5. Surfzone eddies and headland rip VLF fluctuations at a geologically constrained beach

XB-SB was implemented on a regular grid extending 4000 and 10 000 m in the cross-shore $x$ and the longshore $y$ direction, respectively (Fig. 2b). The computational domain comprises morphological features such as offshore bedrock and sand deposit lobe off the river mouth, the Adour dike, and the six groynes along Anglet beaches, PCA, and the Saint Martin headland and the adjacent embayment GPB. The mesh step size was set to 5 m at PCA, gradually increasing to 25 m close to the offshore boundaries (Figs. 2c,d).

Mouragues et al. (2021) describe how the present model was calibrated at the Anglet site using realistic forcing for waves (wave buoy Candhis 06402 moored in 50-m water depth) and water levels collected at a nearby tidal gauge during the energetic event considered here (event D2 on 7 October 2018). In the present study, the VLF fluctuations of the deflection rip are investigated with JONSWAP spectra generated using the mean offshore wave conditions averaged over the considered event ($H_s = 4$ m, $T_p = 10$ s and $\theta_p = -20°$). The peak enhancement factor and the directional wave spreading are set to 3.3° and 24° (XBeach default values). This spectrum is used to force the model for 20 h in order to ensure that a significant number of VLF fluctuations are modeled. To disregard model spinup, the
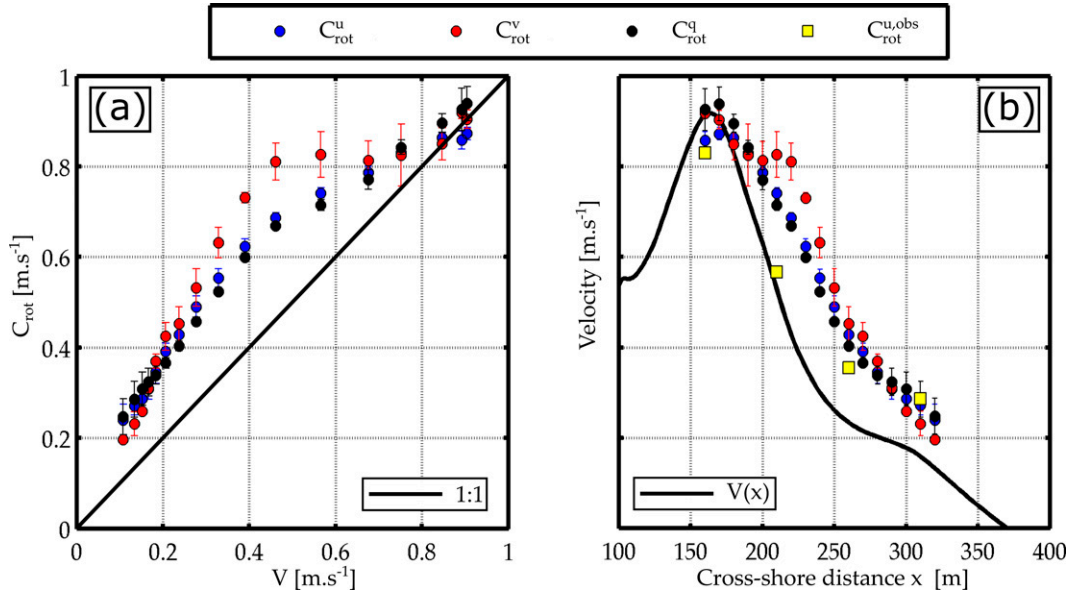
FIG. 6. (a) Eddy celerity $C_{rot}$ extracted from cross-shore velocities (blue; $C_{rot}^u$), longshore velocities (red; $C_{rot}^v$), and vorticity (black; $C_{rot}^q$). (b) Cross-shore profile of rotational velocities (points) and mean longshore current (black line). For both panels, points show the averaged celerities (for different $c_s$ shown in Fig. 4) while vertical bars show the associated standard deviation. In (b), yellow squares show observed eddy celerities extracted from cross-shore velocities ($C_{rot}^{u,obs}$).

last 12 h of the simulation are used for the investigation. The tide elevation is set constant during the entire simulation: $\zeta_{tide} = -2$ m and $\zeta_{tide} = 2$ m for the low tide and high tide simulation, respectively. As previously explained, using

a constant tidal elevation throughout the simulations ensures that surfzone VLF motions are stationary.

Following the model calibration carried out by Mouragues et al. (2021), $\gamma = 0.50$ and $C = 45$ m$^{1/2}$ s$^{-1}$ will be used for the
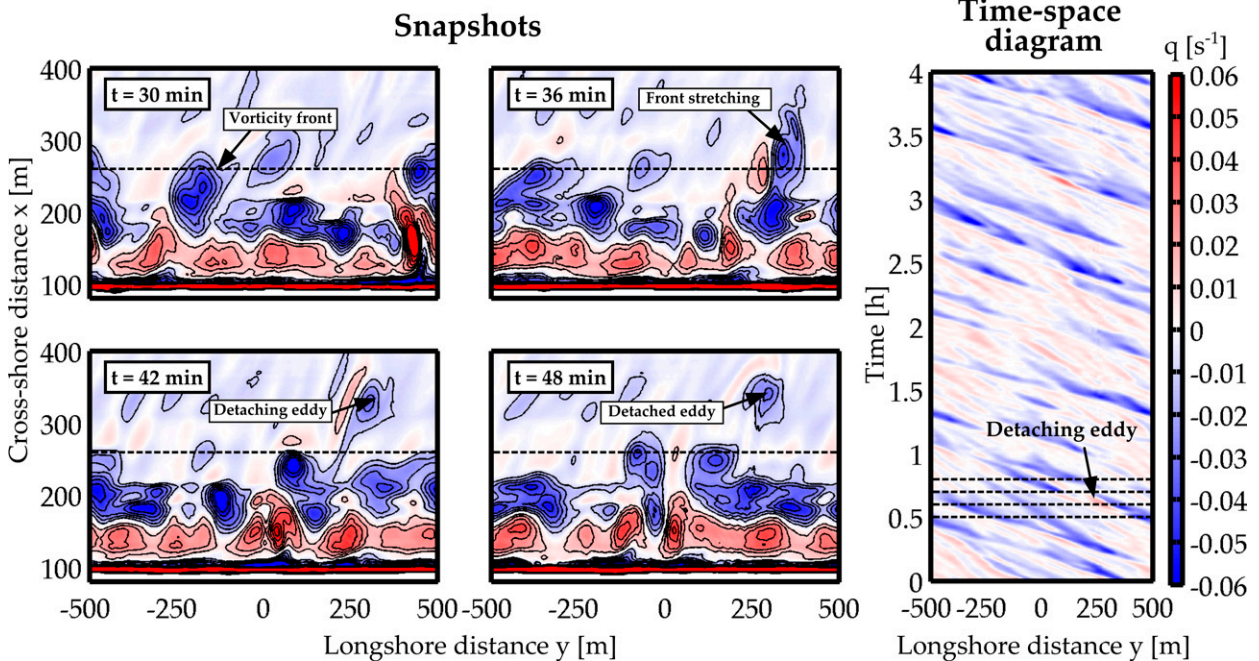


FIG. 7. (left) Snapshots of vorticity at four different times ($t = 30, 36, 42,$ and 48 min) depicting the stretching and the splitting of a vorticity front. The dashed black line corresponds to the cross-shore position $x = 260$ m. (right) Time–space diagram of vorticity along the cross-shore position $x = 260$ m. Dashed black lines correspond to times at which vorticity field is plotted on the left-hand panels. For a better visualization, the reader is referred to vorticity animations (see supplemental material).
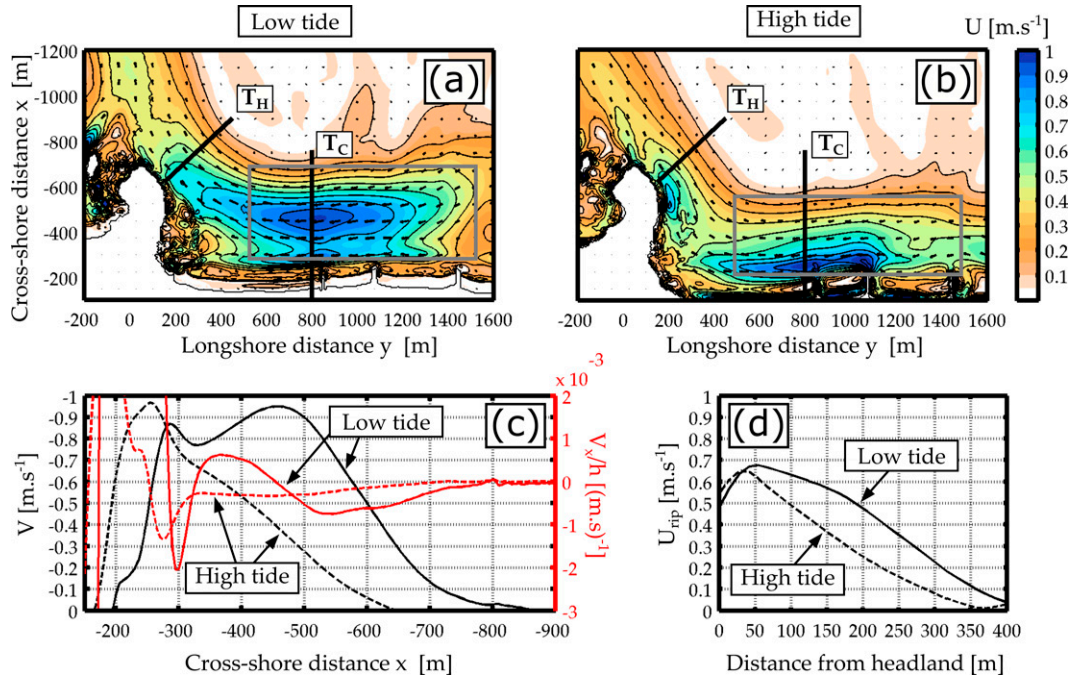
FIG. 8. (a),(b) Mean velocity field at low tide and at high tide. For both top panels, the black line shows two transects along which vorticity is plotted in other figures ($T_C$ is the cross-shore transect of the longshore current, and $T_H$ is the cross-section transect of the deflection rip). The gray rectangle indicates the area where the $k–f$ spectrum is computed. (c) Cross-shore profile of mean longshore current $V$ (black line) and potential vorticity associated with $V$ (red line). (d) Cross-section profile of the mean deflection magnitude $U_{rip}$. For both bottom panels, plain (dashed) lines are for low tide (high tide).

Anglet modeling experiment. Finally, it should be noted that modeled deflection rip velocities in Anglet were found insensitive to the value of $c_s$ (not shown; results are similar to Mouragues et al. 2021). For consistency with the SandyDuck modeling experiment, $c_s$ was set to 1 for all Anglet modeling experiments.

### a. Mean circulation and surfzone eddies

Figures 8a and 8b show the mean velocity field along PCA at low tide and high tide, respectively. The breaking of highly oblique and highly energetic incident waves ($H_s \approx 4.0$ m and $\theta_p \approx 20°$) induces a strong and wide longshore current $V$ oriented to the south. The latter is deflected seaward against the headland, creating a deflection rip extending hundreds of meters off the headland tip. At low tide, the surfzone width is similar to the headland length and the longshore current is deflected by the headland and by the adjacent embayment flow (Mouragues et al. 2021).

The surfzone morphology of PCA is relatively longshore-uniform with a relatively steep upper beach face and a low tide terrace that can be exposed at low tide. For a given incident wave condition, changes in tidal elevation alter the pattern and intensity of depth-induced breaking wave energy dissipation which, in turn, results in a strong tidal modulation of the cross-shore distribution of the longshore current along PCA (Fig. 8c). At low tide, the longshore current is wide and

has two local maxima. The highest maxima are located seaward at $x = -450$ m and reaches 0.95 m s$^{-1}$. At high tide, the main peak moves shoreward at $x = -250$ m and reaches 0.98 m s$^{-1}$. The mean seaward shear is around 0.0027 s$^{-1}$ for both tide levels, which is less than half of the longshore current shear during the SandyDuck experiment. For each longshore current profile $V$, its potential vorticity $V_x/h$ is shown and displays at least one local extremum which is a necessary condition for a shear instability to exist (Bowen and Holman 1989; Dodd et al. 1992). Because the longshore current peak is closer to the shoreline at high tide than at low tide, the location along the headland at which the longshore current is deflected offshore is also closer to the shoreline. This leads to a more concentrated, slightly more intense and narrower seaward flowing jet against the headland at high tide. Along $T_H$, the headland rip flow is around 50–100 m wider at low tide than at high tide (Fig. 8d).

Wavenumber–frequency spectra of vorticity at different cross-shore positions in the surf zone and for both tide levels are shown in Fig. 9. Similar to the SandyDuck experiment, the presence of SZE propagating in the same direction as the longshore current along PCA is ubiquitous. The approximative range of energetic frequencies is centered around 2 mHz (8 min) and decreases seaward with, for instance, much lower energy for $f > 5$ mHz at $x = -600$ m ($x = -370$ m) than at $x = -500$ m ($x = -270$ m) for low tide (high tide). By contrast, $k–f$ spectra suggest that the range of energetic
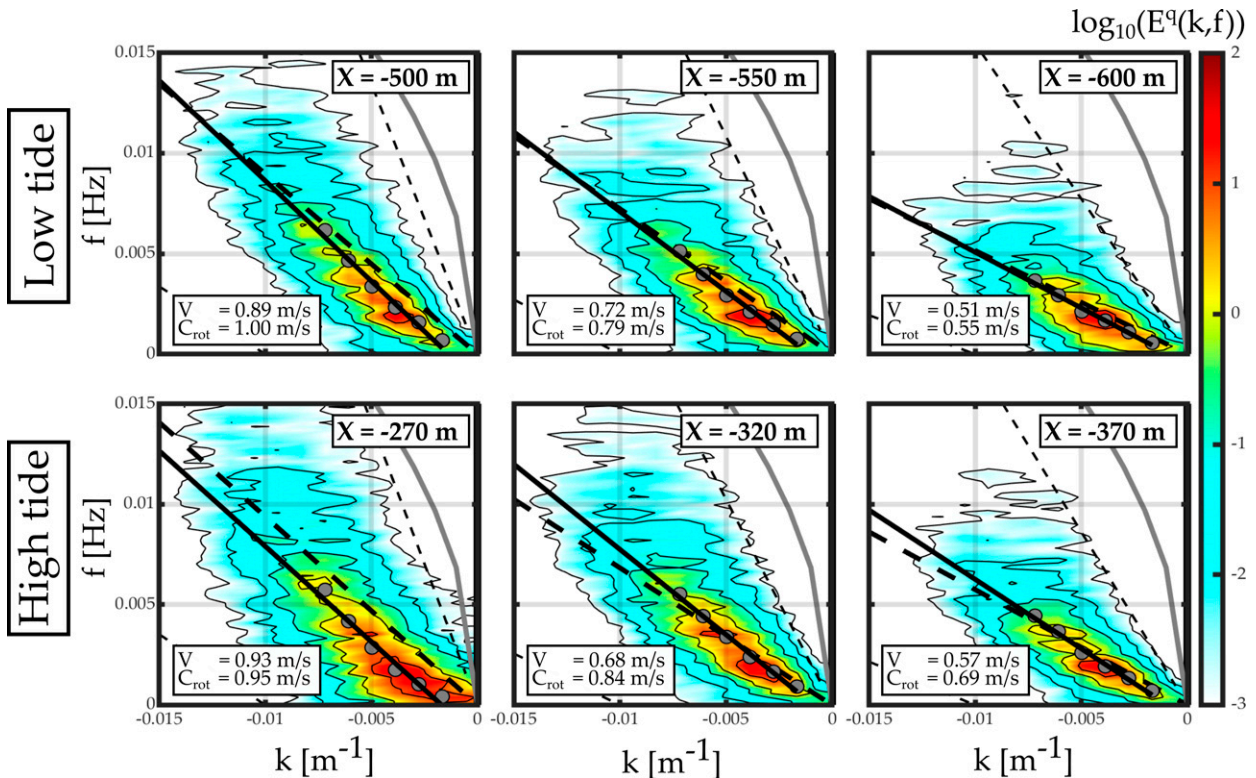
FIG. 9. Modeled wavenumber–frequency spectra of vorticity $q$ $[E^q(k, f)]$ at (top) low tide and (bottom) high tide extracted at different cross-shore positions $x$. For each panel, the local value of the mean longshore current $V$ and the estimated eddy celerity $C_{rot}$ are written. The definition of multiple dispersion lines is the same as in Fig. 3b.

wavenumber remains relatively constant with cross-shore positions and is centered around 0.004 m$^{-1}$ (250 m). The estimated celerity decreases seaward, going from $O(1)$ m s$^{-1}$ near the longshore current peak to $O(0.1)$ m s$^{-1}$ 500 and 700 m offshore at high tide and low tide, respectively (see Fig. 10). It should be noted that the estimation of the eddy celerity is relatively sensitive to the method to fit the straight dispersion line (Özkan-Haller and Kirby 1999). Such sensitivity is enhanced in Anglet which setup (morphology, high-energy wave conditions) is more complex than along the longshore-uniform sandy beach of Duck. This complexity, in addition to eddy interactions, may strongly increase discrepancies between the estimated eddy celerity and the local mean longshore current. To increase the accuracy of the estimated eddy celerity, points $(k, f_{rot})$ with energy less than three orders of magnitude of the energy peak were removed from the fitting procedure. The resulting eddy celerity and the mean current have equivalent trends which is similar to SandyDuck.

Concluding this section, model results indicate the presence of SZE along PCA at both low tide and high tide. These eddies propagate in the direction of the longshore current and their celerity decreases seaward which is similar to Sandy-Duck (see section 4). In the next section, the model is used to explore the relationship between such eddies and the VLF fluctuations of the deflection rip.

### b. Surfzone eddies and headland rip fluctuations

To investigate the hydrodynamic connections between the surf zone and the deflection rip, time–space and frequency–space diagrams of vorticity are computed along a transect in the surfzone $T_C$ and against the headland $T_H$ (see Figs. 8a,b for transect location). These diagrams are shown in Fig. 11 at low tide. Associated with those, Fig. 12 shows several snapshots of vorticity which emphasize the length scales of vorticity fronts, their longshore advection, their merging and their offshore shedding through the deflection rip.

In the surf zone, two vorticity front pairs are present (Fig. 12) and are associated with the two local maxima of longshore current at low tide (see Fig. 8c). The seaward vorticity front pair is characterized by intense negative vorticity fronts that span the entire seaward longshore current region, going from around $x = -550$ m to $x = -870$ m. In this region, the frequency–space diagram along the cross-shore transect in the surfzone $T_C$ (top-right panel in Fig. 11) highlights energetic frequencies that are similar to frequencies of SZE detected previously. Each cross-shore position is characterized by a relatively narrow range of energetic periods. Energetic periods of 5–8 min dominate the spectrum just seaward of the peak while periods of 30 min and 1 h dominate the spectrum further offshore.

In this locally alongshore-uniform surfzone situation, the most energetic period increases with the distance to the location of the longshore current peak (see top-right panel in Fig. 11).
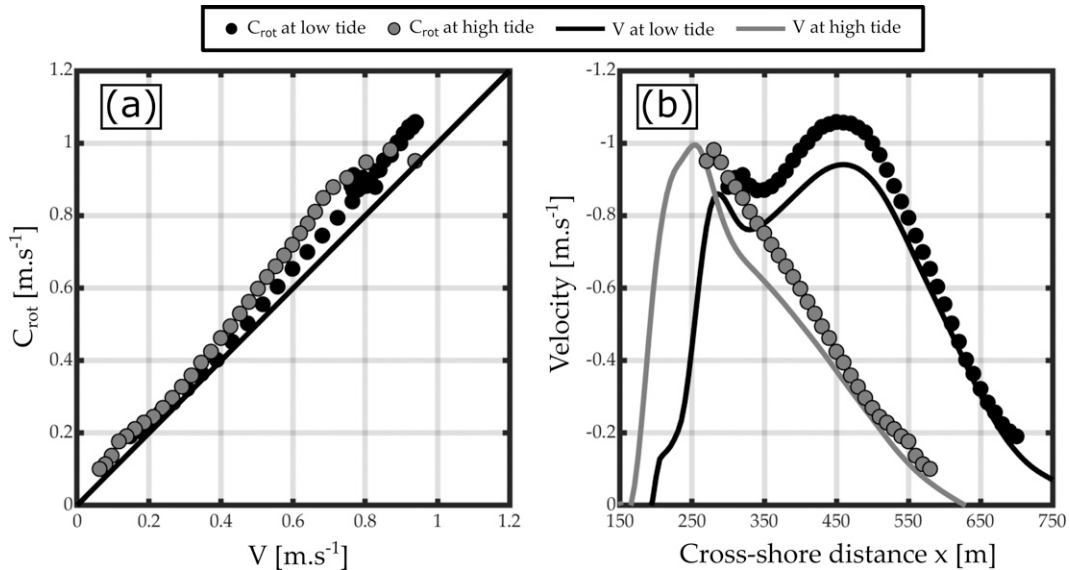
FIG. 10. (a) Eddy celerity $C_{rot}$ extracted from vorticity vs local value of mean longshore current $V$. (b) Cross-shore profile of eddy celerities (points) and mean longshore current (line). Black and gray are for low tide and high tide, respectively.

As suggested above, the most energetic longshore wavelength may remain relatively constant across the surf zone, indicating that the spatial structure of the corresponding eddies are conserved while their propagation speed decreases seaward. The latter mechanism can force the splitting of some vorticity fronts, leading to the generation of detached eddies that can propagate off the surf zone. This is better emphasized in the vorticity animation (see supplemental material) and vorticity snapshots shown in Fig. 12. Vorticity fronts span the entire surf zone and are advected by the longshore current. The most shoreward part of a front propagates faster than the seaward part, which forces front stretching and detaching eddies. These eddies can flow off the surf zone or merge with the following front. Such mechanisms can also explain the differences between the representative eddy celerity and the mean longshore current (Fig. 6).

Close to the headland, these fronts are expelled offshore through the deflection rip against the headland. Frequency–space diagrams along $T_C$ and $T_H$ are relatively similar, suggesting that fluctuations in the deflection rip are associated with the deflection of the upstream SZE. Along the cross section of the rip neck $T_H$, energetic periods ranging from 5 min to 1 h dominate the spectrum. Far from the headland, only fluctuations with energetic periods of around 42 min dominate the spectrum at SIG1 location, which is similar with measurements (see Fig. 2 and Mouragues et al. 2021).

Similar to low tide, the spatiotemporal (frequency) variability of vorticity at high tide is shown in Figs. 13 and 14. The frequency–space diagram of vorticity along $T_C$ is relatively similar to the one at low tide, with energetic periods that essentially increase seaward. At high tide, the mean longshore current has also two local maxima which are associated with two vorticity front pairs in the surf zone (see around $x = -280$ m and $x = -500$ m). Just seaward of the main peak located at

$x = -270$ m, intense negative vorticity fronts are advected along the stream with energetic periods of around 5 min. Further offshore, the longshore current profile displays a secondary bump (see around $x = -420$ m) and is associated with vorticity fronts propagating slower than the shoreward fronts, with energetic periods around 30 min.

The examination of vorticity animation at high tide (see supplemental material) suggests that vorticity fronts merge at the location where the longshore current starts to be deflected offshore (region around $x = -400$ m and $y = 400$ m). The merged fronts are then expelled offshore through the deflection rip which leads to a much narrower range of energetic periods along $T_H$ than along $T_C$, with distinct energetic periods of 23 and 50 min along $T_H$ (see bottom-right panel in Fig. 13). The latter model result differs with the low tide simulation which highlighted the relatively same range of energetic periods along $T_C$ and $T_H$.

This is believed to be controlled by the relative difference of mean flow patterns between low tide and high tide. At high tide, the mean flow against the headland is concentrated within a narrower region than at low tide (Fig. 8). This allows all surfzone vorticity fronts to pass through the deflection rip at low tide while, at high tide, some surfzone fronts may merge together before being expelled offshore by the rip. This leads to energetic higher periods against the headland that were not necessarily present updrift in the surf zone (Fig. 13). This mechanism will be further discussed in section 6.

## 6. Discussion

In the following section, some components of the above model results are discussed and suggestions for future works are proposed. The morphological control on headland rip
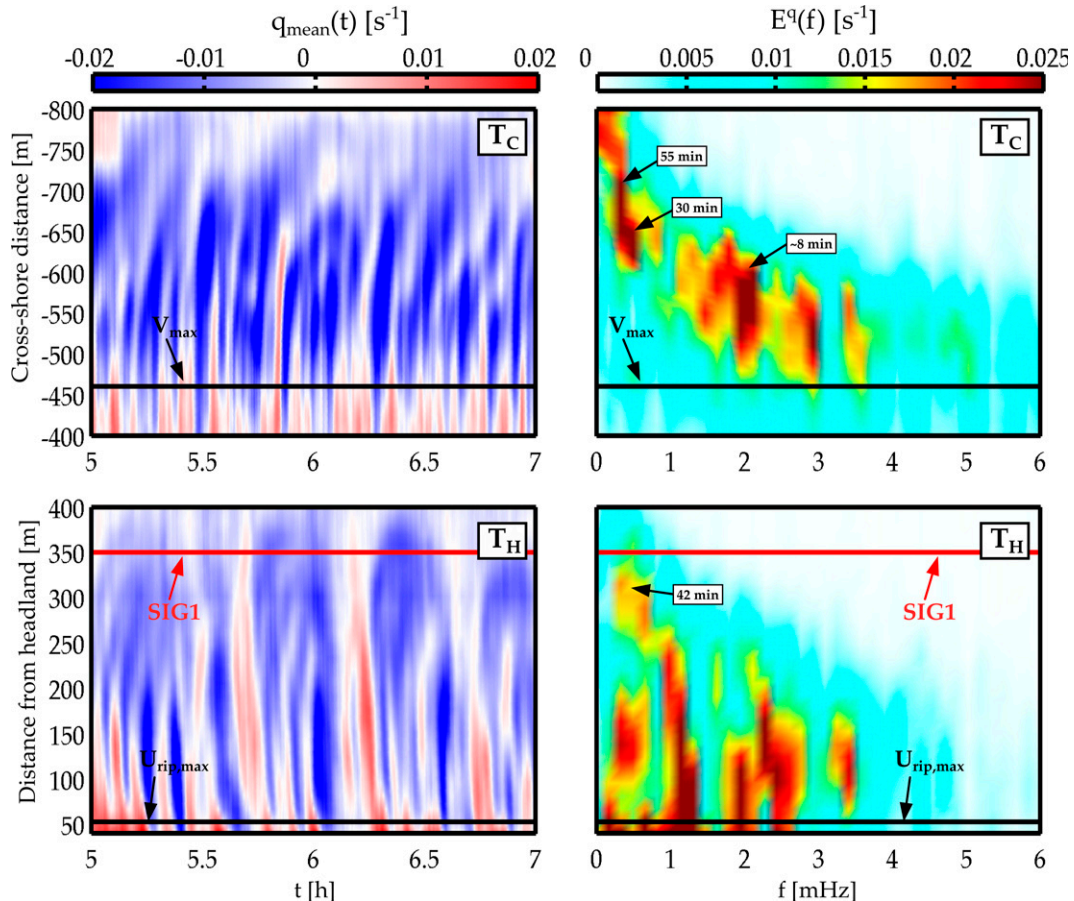
FIG. 11. (left) Time–space diagram of 100-s running averaged vorticity $[q_{mean}(t)]$ and (right) frequency–space diagram of instantaneous vorticity spectrum $[E^q(f)]$ along two transects at low tide (see Fig. 8a for transect location). (top) Transect $T_C$ with the black line indicating the mean longshore current peak position. (bottom) Transect $T_H$ with the black (red) line indicating the mean deflection rip peak (SIG1) position.

VLF fluctuations, through idealized morphology, is first explored. The latter will be critical to support the fact that the headland may enforce the merging of surfzone eddies as previously highlighted at PCA at high tide. Then, the role of wave group forcing and shear instability processes on surfzone rotational motions is discussed. In particular, we will point out the essential role of incident wave groups to produce surfzone eddies under high-energy oblique wave conditions. The latter will raise forward the discussion on a continuum of the driving mechanism of surfzone rotational motions under obliquely incident waves.

### a. Morphological control on headland rip VLF fluctuations

In section 5, the spatiotemporal variability of vorticity suggests that fluctuations of the rip are associated with the propagation of eddies along the deflection stream. For a given headland length, the reduction of the surfzone width can strongly modify the mean headland rip flow, with a more concentrated seaward jet flow as surfzone width decreases. This forces the merging of vorticity fronts near the headland which

results in energetic higher periods against the headland that were not necessarily present in the surf zone. To further analyze this mechanism, the model is run on an idealized morphology which is made of a planar surfzone morphology (constant slope of 0.03) and a physical boundary (headland) with a given length $L_g$. The incident wave conditions are the same for all modeling experiments ($H_s = 2$ m and $\theta = -20°$). These conditions result in a 200-m-wide longshore current (surfzone width $X_b \approx 200$ m) peaking around 0.8 m s$^{-1}$ (Fig. 15a). To obtain different mean flow patterns and further emphasize their effects on the energetic periods, $L_g$ is varied so that the boundary length to surfzone width ratio $L_g/X_b$ varies from 0.3 to 1.2. This allows to model the full spectrum of mean deflection patterns, going from weakly to strongly deflected longshore current (Scott et al. 2016). With a constant $X_b$, the mean flow patterns feature different deflection rip widths (see left panels in Fig. 15). It should be noted that obtaining flow patterns with different surfzone and deflection rip widths could have also been done with e.g., varying tidal level (as previously done in Anglet; see section 5) or varying offshore wave conditions (varying $X_b$). Here, we choose to vary $L_g/X_b$ for consistency with Scott et al. (2016). These
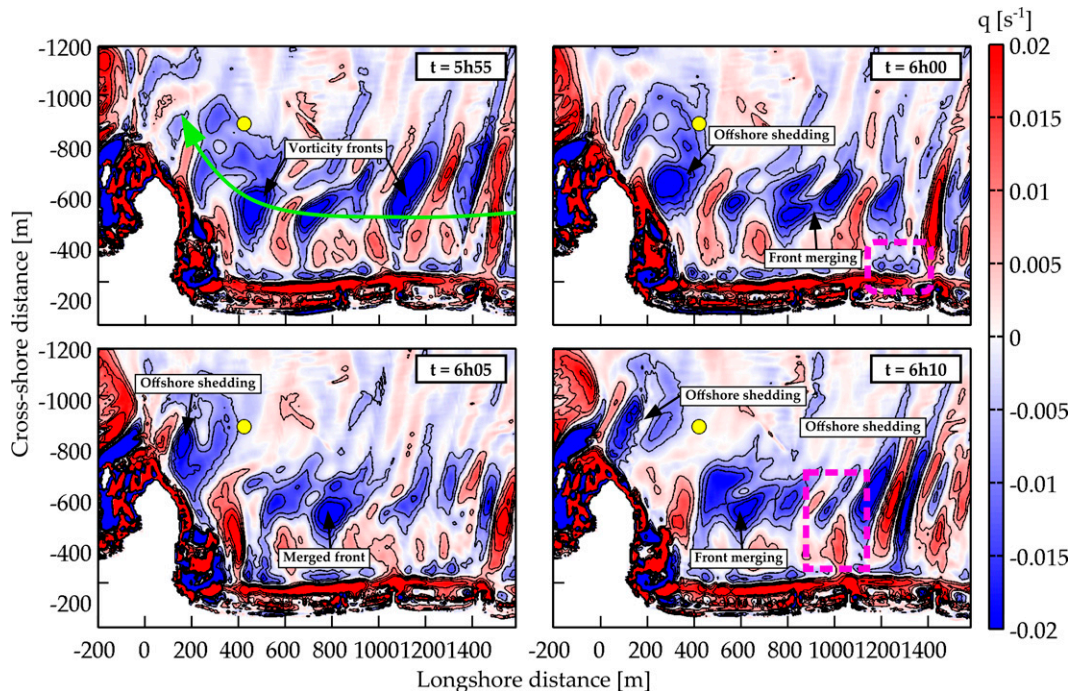
FIG. 12. Snapshots of vorticity at low tide at four different times showing stretched vorticity fronts, front interactions and offshore shedding through the deflection rip. The yellow point indicates the SIG1 location, and the green arrow in the top-left panel shows the main propagation direction of vorticity fronts. Dashed magenta rectangles show an example of two vorticity front pairs. For a better visualization, the reader is referred to vorticity animations (see supplemental material).

authors have varied this ratio to highlight the different deflection mean (time-averaged) flow patterns. The present model experiments aim at extending their work at the VLF scales.

For each experiment, the time–space (frequency) diagrams of vorticity along two transects ($T_C$ and $T_H$) are presented (see center and right panels in Fig. 15). Note that the same incident infragravity wave phases were used to run the model so that the variability of vorticity in the surf zone (transect $T_C$) is similar for all experiments. The latter vorticity variability is shown in Figs. 15b and 15c. The other center and right-hand panels show vorticity along transect $T_H$ for all experiments and highlight the effect of varying $L_g$ (or $L_g/X_b$) and, in turn, the deflection rip width on the range of energetic periods in the deflection rip. As $L_g/X_b$ increases, the deflection rip is compressed within a narrow region and its width is much shorter than the surfzone width (see left-hand panels). The range of energetic periods in the deflection rip strongly decreases compared to the range of energetic periods in the longshore current. For the longest boundary ($L_g/X_b = 1.2$), only periods higher than 7 min dominate the deflection rip spectrum (Fig. 15r) while the longshore current features a wide range of energetic periods, going from 4 to 50 min (Fig. 15c).

Overall, these results underline the previously observed effect that an headland may have on the vorticity motions generated upstream in the surf zone. This is better emphasized by the continuous peak frequency $f_{p,vlf}$ computed as $\int f[E^q(f)]^4 df / \int [E^q(f)]^4 df$ (see right-hand panels). As $L_g/X_b$ increases, the cutoff frequency

($f_{p,vlf}$ closest to the headland) decreases from 2.5 to 1.75 mHz for $L_g/X_b = 0.3$ and 1.2, respectively (Figs. 15f and 15r, respectively). The peak frequency also strongly decreases with the distance from headland $x_h$. To further synthesize this mechanism, Fig. 16 shows $T_{p,vlf} = 1/f_{p,vlf}$ at two different $x_h$ as a function of $L_g/X_b$ and for different $H_s$ in order to highlight the effect of varying $X_b$. Both $X_b$ feature similar period patterns. As $L_g/X_b$ increases, periods at both positions and the period gap between both positions increase, which illustrates the effect of the headland on energetic periods.

### b. Effects of wave-group forcing on vorticity dynamics

The effect of wave forcing, through breaking wave vorticity forcing, on the characteristics of surfzone rotational motions under obliquely incident wave conditions has been addressed by very few studies (e.g., Long and Özkan-Haller 2009; Feddersen 2014). In the above modeling analysis, the term "shear waves" was sometimes used, for simplicity, to refer to surfzone rotational motions in the presence of a longshore current $V$. This could mask the fact that shear instabilities of $V$ are not the only driving mechanism of such motions. Under obliquely incident wave conditions, surfzone eddy generation mechanisms include shear instabilities of $V$ (hereafter referred to as SI; e.g., Bowen and Holman 1989) and breaking wave vorticity forcing at the wave group scale (hereafter referred to as WG; e.g., Long and Özkan-Haller 2009) and at the individual wave scale through along-crest variation in wave dissipation (hereafter referred
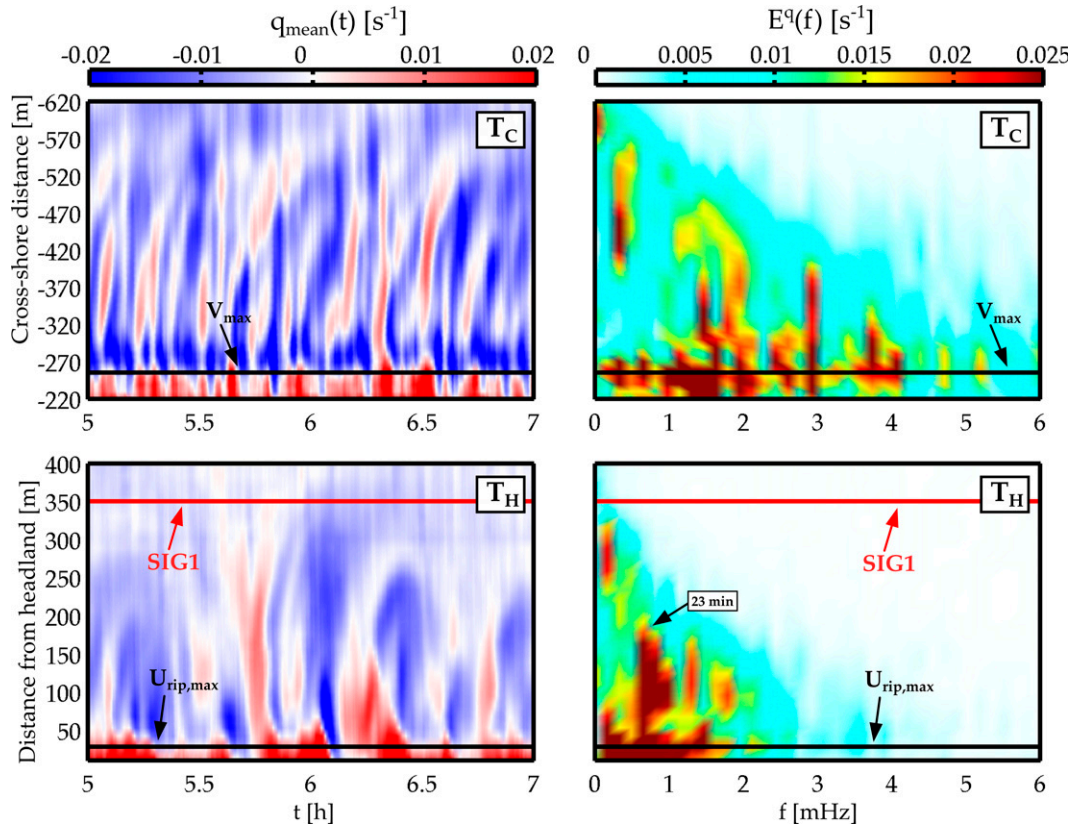
FIG. 13. (left) Time–space diagram of 100-s running averaged vorticity [$q_{mean}(t)$] and (right) frequency–space diagram of instantaneous vorticity spectrum [$E^q(f)$] along two transects at high tide (see Fig. 8b for transect location). (top) Transect $T_C$ with the black line indicating the mean longshore current peak position. (bottom) Transect $T_H$ with the black (red) line indicating the mean deflection rip peak (SIG1) position.

as IW; e.g., Peregrine 1998; Feddersen 2014). Understanding the relative importance of each mechanism is essential to effectively predict surfzone rotational motions which strongly control mixing processes in the nearshore (e.g., Spydell et al. 2007; Clark et al. 2012).

A WG-resolving model allows simulating surfzone rotational motions driven by both WG and SI. Long and Özkan-Haller (2009) showed that the vorticity production due to WG was dominant compared to SI under weakly oblique incident wave conditions ($\theta = 8°$), while production due to WG and SI was similar under strongly oblique incident wave conditions ($\theta = 20°$). In line with Long and Özkan-Haller (2009), excluding WG for the SandyDuck experiment (strong shear; Fig. 5a) resulted in weaker rotational motions while excluding WG for the Anglet experiment (weak shear; Fig. 8c) resulted in the absence surfzone eddies (not shown).

This suggests the existence of a continuum in the driving mechanisms of surfzone rotational motions under obliquely incident waves, from fully WG-driven motions for weakly sheared $V$ to both WG- and SI-driven motions for $V$ with stronger shear. Note that Feddersen (2014) used a wave-resolving model to investigate eddy generation due to all three mechanisms described above (SI, WG, and IW). The existence of a continuum

was suggested but was not fully illustrated. Importantly, this continuum would further point out the critical role of WG to produce surfzone eddies under high-energy and oblique wave conditions.

To illustrate such continuum, the model is run onto the barred beach of the SandyDuck experiment with varying wave angle of incidence $\theta$. It should be noted that a barred beach was necessary, as opposed to a planar beach, to obtain a sheared-enough $V$ so that eddies are generated when excluding WG. Simulations excluding and including WG are made for $\theta$ ranging 0°–40° leading to longshore currents with a wide range of peak magnitude $V_{max}$ (Fig. 17a). The associated $k$–$f$ vorticity spectra emphasize how wave group forcing broadens the spectrum (Fig. 17b). Energetic frequencies and wavenumbers are concentrated within a very narrow ridge when excluding WG while the energy is much scattered when including WG. For normally incident waves, surfzone eddies are absent when WG are excluded, emphasizing the essential role of WG to produce eddies for weakly oblique waves.

This is better illustrated by plotting the total vorticity variance as a function of $\theta$ [$(\sigma_{q,rot})^2$ and $(\sigma_{q,sw})^2$ including and excluding WG, respectively; Fig. 17c]. For $\theta < 30°$, $(\sigma_{q,rot})^2$ is at least 2 times higher than $(\sigma_{q,sw})^2$, indicating that WG forcing
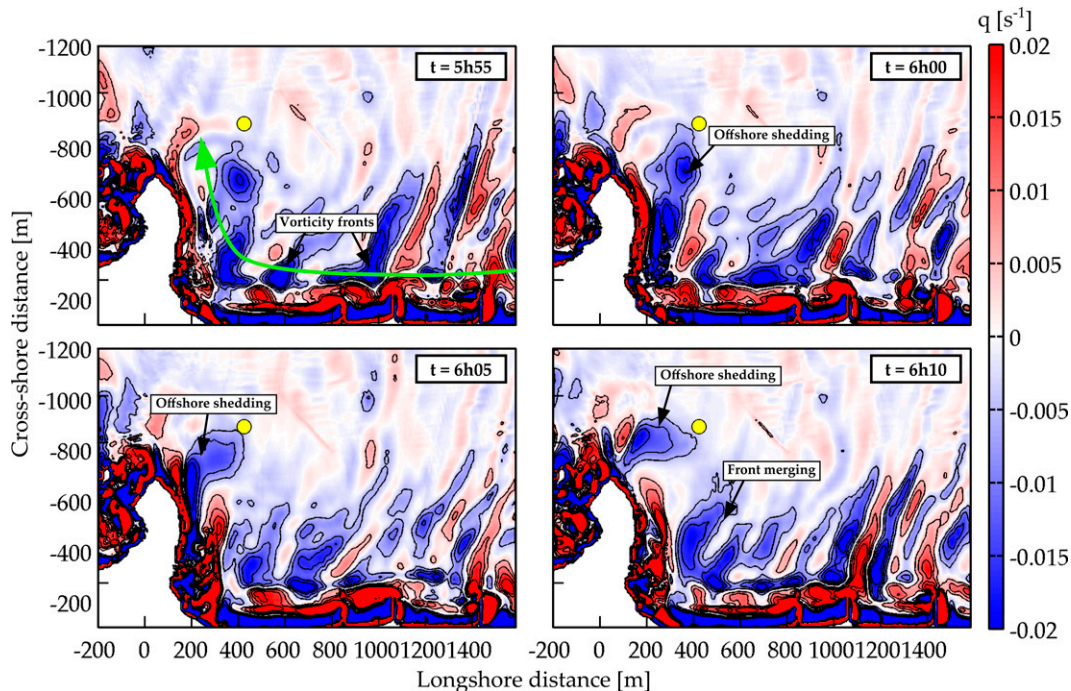
FIG. 14. Snapshots of vorticity at high tide at four different times and showing stretched vorticity fronts, front interactions, and offshore shedding through the deflection rip. Yellow point indicates SIG1 location and the green arrow in the top-left panel shows the main propagation direction of vorticity fronts. For a better visualization, the reader is referred to the vorticity animations (see supplemental material).

is responsible for at least 50% of vorticity variance. For $\theta$ between $0°$ and $25°$, $(\sigma_{q,\mathrm{rot}})^2$ increases until reaching a maximum at around $\theta = 25°$. For $\theta > 25°$, $(\sigma_{q,\mathrm{rot}})^2$ decreases which highlights the decreasing contribution of WG to surfzone eddies. This decreasing trend may be due to the modification of the longshore structure of wave groups as a result of strong wave refraction, therefore modifying the longshore variability of wave forcing and momentum injected in the surf zone. Further modeling works will be required to confirm the latter suggestion.

For $\theta$ between $0°$ and $25°$, $(\sigma_{q,\mathrm{sw}})^2$ linearly increases until reaching a plateau for $\theta > 25°$, suggesting that the SI contribution reaches a saturation. Note that Figs. 17b–d were plotted at a given cross-shore location $x = -200$ m but similar trends were obtained with other cross-shore locations. The SI contribution saturation may be explained by the fact that the local longshore current shear $V_x$ and the local curvature $V_{xx}$, which controls the SI contribution to surfzone eddy field (see, e.g., Long and Özkan-Haller 2009; Feddersen 2014), becomes relatively steady for strongly oblique incident waves. Note that the presence of more energetic surfzone eddies when WG are included leads to more cross-shore mixing, compared to when WG are excluded, which smooths the longshore current profile (Fig. 17a). Discrepancies between both variances decreases as $\theta$ increases, suggesting the decreasing contribution of WG, compared to SI, as waves becomes more oblique, which is in line with Long and Özkan-Haller (2009).

The relative balance between SI and WG contribution to surfzone eddies is well emphasized by plotting the vorticity variance ratio $\{[(\sigma_{q,\mathrm{rot}})^2 - (\sigma_{q,\mathrm{sw}})^2]/(\sigma_{q,\mathrm{rot}})^2\}$ as a function of the mean seaward shear $\tau$ (Fig. 17d). The latter is defined as $V_{\max}/\Delta$, where $\Delta$ is the seaward width, computed from $V(x)$ including WG (see plain lines in Fig. 17a). For the lowest $\tau$ ($\tau < 0.004\,\mathrm{s}^{-1}$), this ratio is always higher than 0.8, indicating that WG forcing is the main eddy generation mechanism. The mean seaward shear for the Anglet experiment (see blue text in Fig. 17d) falls within the lowest range of $\tau$, suggesting that surfzone vorticity motions and, in turn, VLF fluctuations of the deflection rip may be primarily driven by WG rather than SI. For higher $\tau$, the SI contribution to surfzone eddies increases, with the variance ratio dropping below 0.6. This indicates that both SI and WG force surfzone eddies. Finally, for $\tau > 0.008\,\mathrm{s}^{-1}$ ($\theta \geq 35°$), the ratio is close to 0, suggesting that WG do not substantially contribute to the total vorticity variance.

Overall, Fig. 17d suggests the existence of a continuum in the surfzone eddy generation mechanisms, from fully WG-driven eddies for low $\tau$ to both WG- and SI-driven eddies for high $\tau$. This is in general agreement with Feddersen (2014), who pointed out the fact that surfzone eddies are primarily controlled by breaking wave vorticity forcing, with possible exceptions for very narrow-banded highly oblique wave conditions. Here, the total vorticity variance was used, as a first approximation, to quantify the relative importance of SI and WG contribution to surfzone eddy generation. However, such
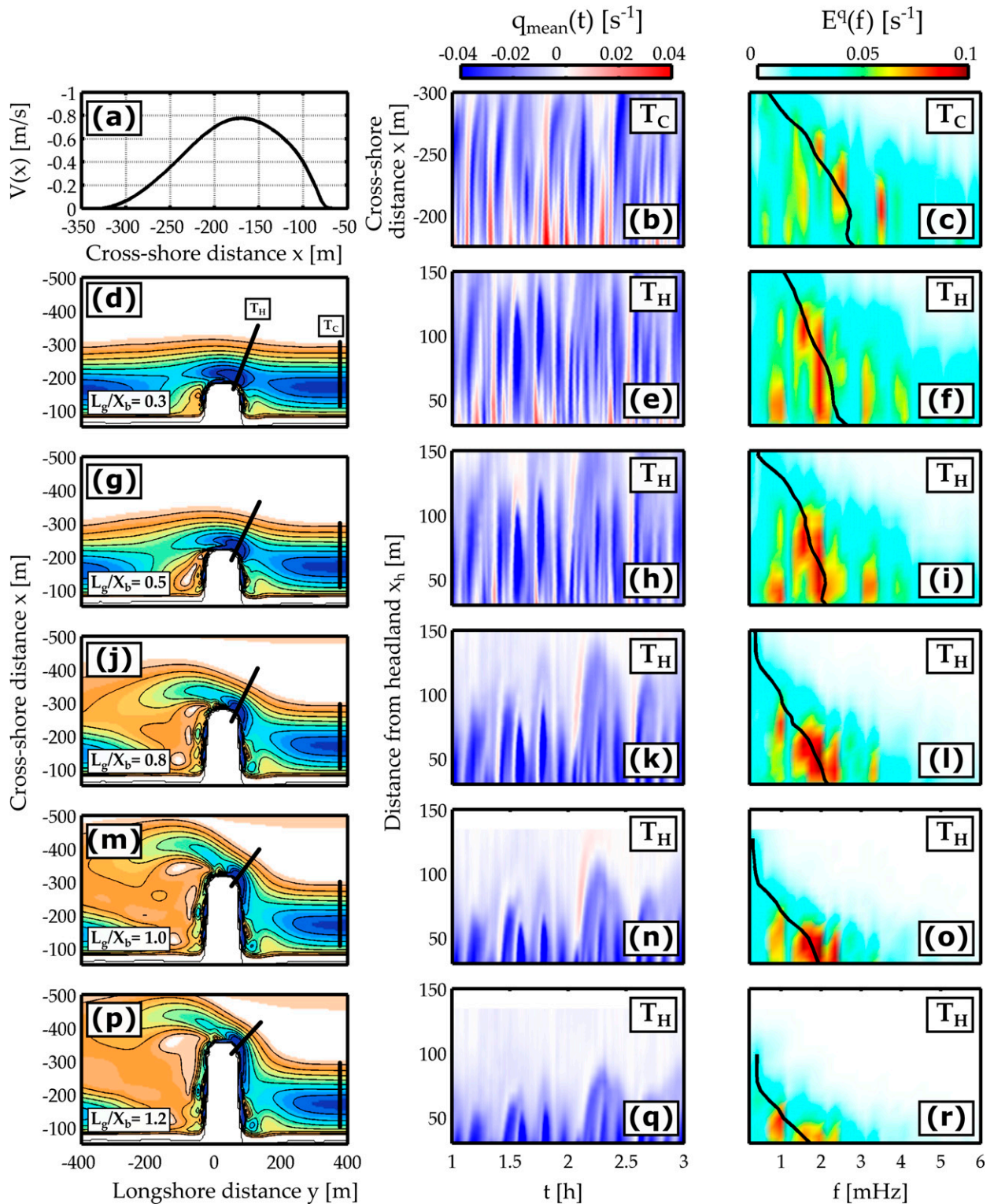
FIG. 15. (left) Mean circulation patterns for different idealized boundary length. The boundary length to surfzone width ratio $L_g/X_b$ is indicated for each panel ($X_b \approx 200$ m). Transects $T_H$ and $T_C$ are indicated in each panel. (center) Time–space diagram of running-averaged vorticity along $T_H$ for different $L_g/X_b$. (right) Frequency–space diagram of instantaneous vorticity along $T_H$ for different $L_g/X_b$. The center top panel (top right panel) shows the time (frequency)–space diagram of running-averaged (instantaneous) vorticity along $T_C$, which is the same for each modeled case (same incident wave phase time series). Black lines in the right panels show the continuous peak frequency $f_{p,\text{vlf}}$ computed as $\int f[E^q(f)^4]df / \int [E^q(f)^4]df$.
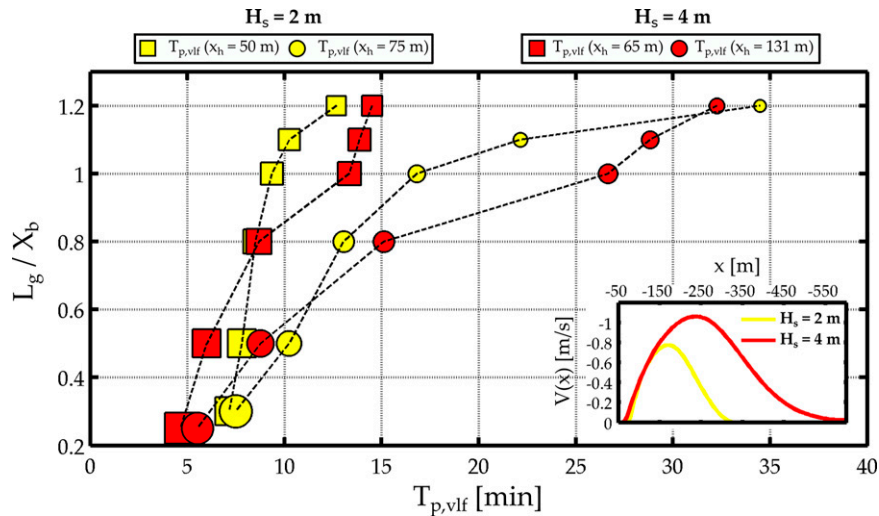
FIG. 16. VLF peak periods $T_{p,\text{vlf}}$ as a function of the boundary length to surfzone width ratio $L_g/X_b$. Yellow and red are for $H_s = 2$ m ($X_b = 200$ m) and for $H_s = 4$ m ($X_b = 400$ m). The $T_{p,\text{vlf}}$ is shown at two different distances from the boundary $x_h$, corresponding to the distance of maximum vorticity variance (50 and 65 m; colored squares) and further away from the boundary (75% of the deflection rip width of the narrowest deflection rip which is for $L_g/X_b = 1.2$; colored circles). The size of squares and sizes is proportional to the vorticity variance, with large and small points associated with strongly and weakly fluctuating vorticity. For each $H_s$, the longshore current profile $V(x)$ is also shown.

bulk quantity does not account for the frequency and wave-number spreading of the vorticity energy. As observations generally report strongly scattered $k$–$f$ spectra (e.g., Özkan-Haller and Kirby 1999; Noyes et al. 2004), the inclusion of breaking wave vorticity forcing is essential to accurately model the full range of surfzone eddies, even for strongly sheared current.

## 7. Summary and future works

A wave-group-resolving model was implemented to investigate the driving mechanisms and the spatiotemporal variability of VLF fluctuations of a deflection rip flowing against a 500-m rocky headland located along Anglet beaches (southwest France). These energetic fluctuations were measured 800 m offshore during a 4-m oblique wave event and had dominant periods of around 1 h and 30 min. The model was first used to simulate surfzone eddies (SZE) in the presence of a longshore current $V$ at a longshore-uniform sandy beach under moderate wave conditions (SandyDuck). This first modeling experiment ensured that the model was able to reproduce characteristics of measured SZE propagating along a strongly sheared current. The spectral signature and the spatiotemporal variability of surfzone rotational motions, which included shear-instability-driven SZE, were displayed and qualitatively compared with past studies.

The model was then implemented in Anglet showing the presence of SZE propagating in the same direction as the longshore current at both low tide and high tide. Due to energetic wave conditions, the longshore current was relatively wide and weakly sheared compared to the SandyDuck modeling experiment. SZE spanned the entire seaward width and

propagated toward the headland at a speed proportional to the local longshore current value. The $k$–$f$ spectra indicated that the celerity and the range of energetic periods of these eddies were decreasing seaward. Space–frequency diagrams of vorticity showed that spectral patterns in the surf zone and along the headland were relatively similar, suggesting that VLF fluctuations of the rip are driven by the deflection of upstream SZE.

At low tide, most energetic periods increased with the distance from the headland, going from $O(1)$ to $O(10)$ min very close to the headland to around 40 min to 1 h hundreds of meters away from the headland which is line with measurements. At high tide, the range of most energetic periods in the rip was much narrower than in the surf zone, suggesting that the headland enforces the merging of surfzone eddies resulting in energetic higher periods against the headland. This mechanism was further explored using idealized simulations with varying boundary length to surfzone width ratio $L_g/X_b$. Increasing such ratio was shown to reduce the deflection rip width and to strongly increase most energetic periods of vorticity fluctuations against the headland. These findings have possible implications for sediment transport occurring along headlands. Most morphological studies along idealized-isolated headlands or natural embayed beaches have shown the ability of deflection rips, based on their time-averaged characteristics, to transport sediments offshore and laterally (e.g., McCarroll et al. 2018; Valiente et al. 2020; McCarroll et al. 2021). Here, we show that time-averaged deflection patterns may not be representative of its dynamics as a result of potentially strong VLF fluctuations. These fluctuations may translate into fluctuations of sediment flows which could impact the amount and
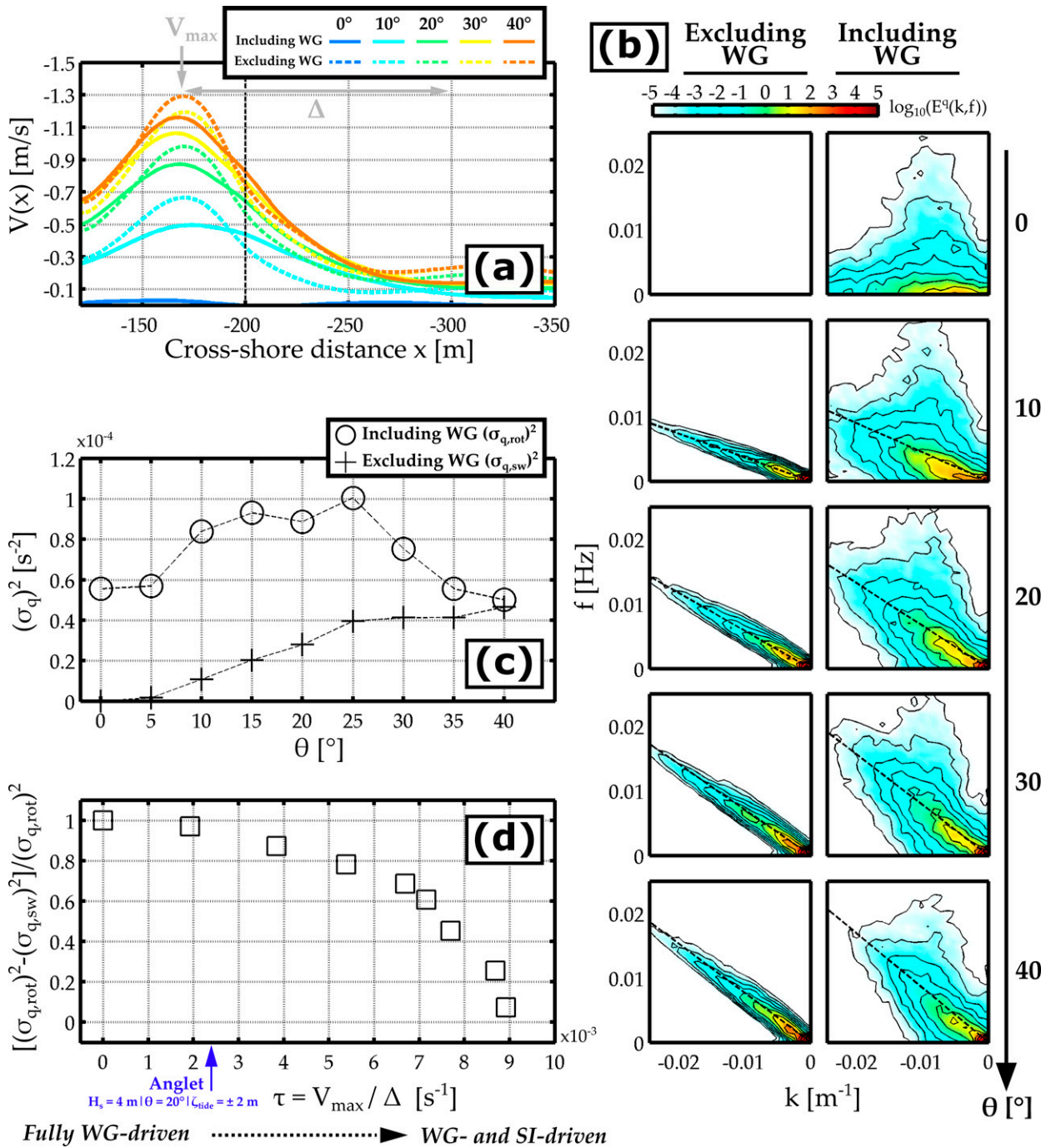
FIG. 17. Surfzone rotational motions modeled including and excluding wave group (WG) forcing for different angle of wave incidence $\theta$ ranging 0°–40°. (a) Cross-shore profiles of mean longshore current $V(x)$. The vertical dashed line shows the cross-shore position at which quantities are plotted in other panels. (b) The $k$–$f$ vorticity spectra computed excluding and including WG for different $\theta$. (c) Vorticity variance as a function of $\theta$, excluding $[(\sigma_{q,sw})^2]$ and including $[(\sigma_{q,rot})^2]$ WG (circle and cross, respectively). (d) Vorticity variance ratio as a function of the mean seaward shear $\tau$ computed as $V_{max}/\Delta$ where $V_{max}$ and $\Delta$ are the peak of $V(x)$ and the seaward width, respectively [see (a)]; $\tau$ for the Anglet model experiments is shown. The dashed horizontal arrow emphasizes the continuum of the surfzone rotational motions driving mechanisms which is discussed in the text (SI is for shear instability).

TABLE A1. Value of each calibrated free parameter for SandyDuck and Anglet experiments.

| Free parameter | Description | Duck | Anglet |
|---|---|---|---|
| $\gamma$ (—) | Breaking parameter | 0.3 | 0.5 |
| $C$ (m$^{1/2}$ s$^{-1}$) | Bottom friction Chezy parameter | 55 | 45 |
| $c_s$ (—) | Horizontal mixing parameter | 1 | 1 |

the spatial dispersion of sediments transported by the rip. Future modeling accounting for sediment transport and morphological changes will unravel the deflection rip-induced sediment transport variability at the VLF scales. In addition to the $L_g/X_b$-dependent deflection patterns, similar idealized simulations with varying headland spacing $L_s$ could be conducted to explore the distance required for longshore currents to develop SZE.

Last, the model was used to assess the effect of wave group forcing on surfzone eddies. Excluding wave group forcing resulted in less energetic eddies for SandyDuck and in the absence of eddies for Anglet, suggesting the existence of a continuum in the driving mechanisms of SZE under obliquely incident waves. To illustrate this continuum, the SandyDuck setup simulation was run with varying wave angle of incidence $\theta$ resulting in longshore currents with different mean seaward shear. Ratio of the total vorticity variance indicates that wave group forcing accounts for more than 50% of the variance for $\theta$ lower than 30°. This suggests that SZE are primarily controlled by breaking wave vorticity forcing rather than shear instabilities, except for strongly oblique wave conditions (strongly sheared current). Interestingly, the contribution of wave groups to the total variance reached a maximum and decreased for $\theta$ higher than 30°. Further works are required to understand how wave groups generate eddies fluctuating at the VLF scale and how their spatial structure impact the eddy variability. Finally, recent studies suggest that low-frequency large-scale surfzone

motions may be the result of a 2D turbulence inverse energy cascade, fed by high-frequency short-scale vorticity motions due to along-crest energy dissipation (e.g., Feddersen 2014; Elgar and Raubenheimer 2020). Future works could address whether vorticity injected at the wave group scale or at the individual wave scale due to the inverse cascade mechanism is more dominant in generating surfzone eddies.

*Data availability statement.* Datasets for this research are included in Mouragues et al. (2020a).

## APPENDIX A

### Calibrated Free Parameters for SandyDuck and Anglet Experiments

Table A1 shows the value of each calibrated free parameter for the SandyDuck and Anglet experiments.

## APPENDIX B

### Wavenumber–Frequency Spectra of Velocities and Vorticity During the SandyDuck Experiment

Figure B1 shows wavenumber–frequency spectra of velocities and vorticity during the SandyDuck experiment.
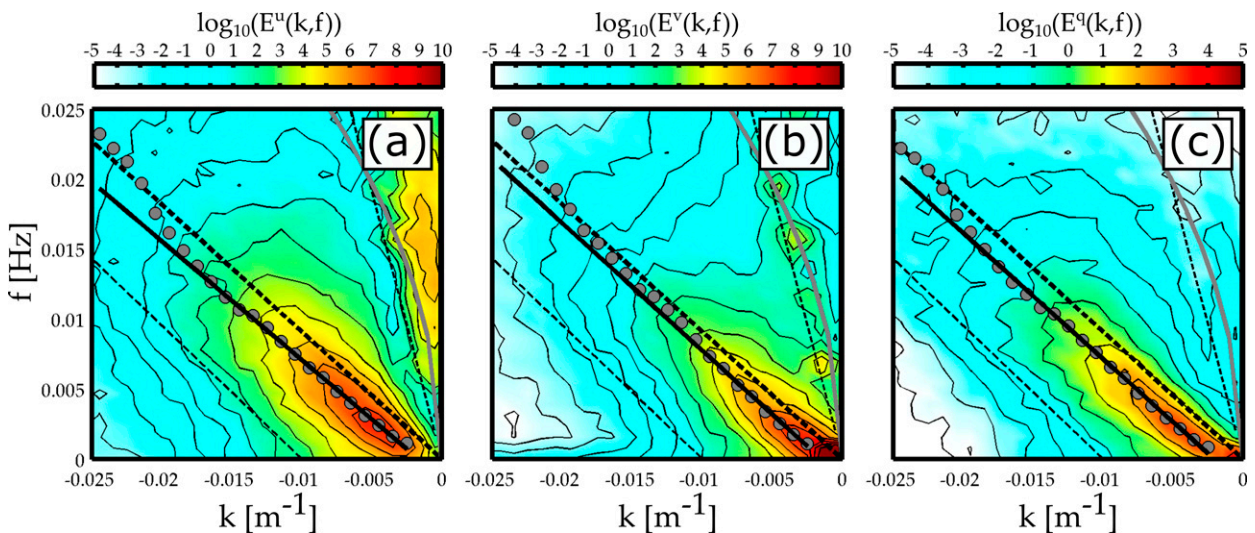


FIG. B1. Modeled wavenumber–frequency spectra of (a) cross-shore velocity $u$, (b) longshore velocity $v$, and (c) vorticity $q$ during the SandyDuck experiment, at the cross-shore position $x = 160$ m. The definition of multiple dispersion lines is the same as in Fig. 3b.

## REFERENCES

Abadie, S., R. Butel, H. Dupuis, and C. Brière, 2005: Paramètres statistiques de la houle au large de la côte sud-aquitaine. *C. R. Geosci.*, **337**, 769–776, https://doi.org/10.1016/j.crte.2005.03.012.

Baquerizo, A., M. Caballeria, M. A. Losada, and A. Falqués, 2001: Frontshear and backshear instabilities of the mean longshore current. *J. Geophys. Res.*, **106**, 16 997–17 011, https://doi.org/10.1029/2001JC900004.

Bowen, A. J., and R. A. Holman, 1989: Shear instabilities of the mean longshore current: 1. Theory. *J. Geophys. Res.*, **94**, 18 023–18 030, https://doi.org/10.1029/JC094iC12p18023.

Castelle, B., T. Scott, R. W. Brander, and R. J. McCarroll, 2016: Rip current types, circulation and hazard. *Earth-Sci. Rev.*, **163**, 1–21, https://doi.org/10.1016/j.earscirev.2016.09.008.

Clark, D. B., F. Feddersen, and R. T. Guza, 2010: Cross-shore surfzone tracer dispersion in an alongshore current. *J. Geophys. Res.*, **115**, C10035, https://doi.org/10.1029/2009JC005683.

——, S. Elgar, and B. Raubenheimer, 2012: Vorticity generation by short-crested wave breaking. *Geophys. Res. Lett.*, **39**, L24604, https://doi.org/10.1029/2012GL054034.

Deigaard, R., E. D. Christensen, J. S. Damgaard, and J. Fredsøe, 1995: Numerical simulation of finite amplitude shear waves and sediment transport. *Coastal Engineering 1994*, B. L. Edge, Ed., American Society of Civil Engineers, 1919–1933, https://doi.org/10.1061/9780784400890.139.

Dodd, N., and E. B. Thornton, 1990: Growth and energetics of shear waves in the nearshore. *J. Geophys. Res.*, **95**, 16 075–16 083, https://doi.org/10.1029/JC095iC09p16075.

——, J. Oltman-Shay, and E. B. Thornton, 1992: Shear instabilities in the longshore current: A comparison of observation and theory. *J. Phys. Oceanogr.*, **22**, 62–82, https://doi.org/10.1175/1520-0485(1992)022<0062:SIITLC>2.0.CO;2.

——, V. Iranzo, and A. Reniers, 2000: Shear instabilities of wave-driven alongshore currents. *Rev. Geophys.*, **38**, 437–463, https://doi.org/10.1029/1999RG000067.

Eckart, C., 1951: Surface waves in water of variable depth. SIO Wave Rep. 100, 99 pp.

Elgar, S., and B. Raubenheimer, 2020: Field evidence of inverse energy cascades in the surfzone. *J. Phys. Oceanogr.*, **50**, 2315–2321, https://doi.org/10.1175/JPO-D-19-0327.1.

Falqués, A., and V. Iranzo, 1994: Numerical simulation of vorticity waves in the nearshore. *J. Geophys. Res.*, **99**, 825–841, https://doi.org/10.1029/93JC02214.

Feddersen, F., 2014: The generation of surfzone eddies in a strong alongshore current. *J. Phys. Oceanogr.*, **44**, 600–617, https://doi.org/10.1175/JPO-D-13-051.1.

Herbers, T. H. C., S. Elgar, and R. T. Guza, 1994: Infragravity-frequency (0.005–0.05 Hz) motions on the shelf. Part I: Forced waves. *J. Phys. Oceanogr.*, **24**, 917–927, https://doi.org/10.1175/1520-0485(1994)024<0917:IFHMOT>2.0.CO;2.

Lippmann, T. C., T. H. C. Herbers, and E. B. Thornton, 1999: Gravity and shear wave contributions to nearshore infragravity motions. *J. Phys. Oceanogr.*, **29**, 231–239, https://doi.org/10.1175/1520-0485(1999)029<0231:GASWCT>2.0.CO;2.

Long, C. E., 1996: Index and bulk parameters for frequency-direction spectra measured at CERC field research facility, June 1994 to August 1995. Miscellaneous Paper CERC-96-6, U.S. Army Engineer Waterways Experiment Station, 142 pp.

Long, J. W., and H. T. Özkan-Haller, 2009: Low-frequency characteristics of wave group–forced vortices. *J. Geophys. Res.*, **114**, C08004, https://doi.org/10.1029/2008JC004894.

Longuet-Higgins, M. S., and R. W. Stewart, 1964: Radiation stresses in water waves; a physical discussion, with applications. *Deep-Sea Res. Oceanogr. Abstr.*, **11**, 529–562, https://doi.org/10.1016/0011-7471(64)90001-4.

MacMahan, J. H., A. J. H. M. Reniers, Ed. B. Thornton, and T. P. Stanton, 2004: Surf zone eddies coupled with rip current morphology. *J. Geophys. Res.*, **109**, C07004, https://doi.org/10.1029/2003JC002083.

McCarroll, R. J., G. Masselink, N. G. Valiente, T. Scott, E. V. King, and D. Conley, 2018: Wave and tidal controls on embayment circulation and headland bypassing for an exposed, macrotidal site. *J. Mar. Sci. Eng.*, **6**, 94, https://doi.org/10.3390/jmse6030094.

——, ——, ——, E. V. King, T. Scott, C. Stokes, and M. Wiggins, 2021: An XBeach derived parametric expression for headland bypassing. *Coastal Eng.*, **165**, 103860, https://doi.org/10.1016/j.coastaleng.2021.103860.

Mouragues, A., P. Bonneton, B. Castelle, V. Marieu, R. J. McCarroll, I. Rodriguez-Padilla, T. Scott, and D. Sous, 2020a: High-energy surf zone currents and headland rips at a geologically constrained mesotidal beach. *J. Geophys. Res. Oceans*, **125**, e2020JC016259, https://doi.org/10.1029/2020JC016259.

——, and Coauthors, 2020b: Field observations of wave-induced headland rips. *J. Coastal Res.*, **95**, 578–582, https://doi.org/10.2112/SI95-113.1.

——, P. Bonneton, B. Castelle, and K. Martins, 2021: Headland rip modelling at a natural beach under high-energy wave conditions. *J. Mar. Sci. Eng.*, **9**, 1161, https://doi.org/10.3390/jmse9111161.

Noyes, T. J., R. T. Guza, S. Elgar, and T. H. C. Herbers, 2004: Field observations of shear waves in the surf zone. *J. Geophys. Res.*, **109**, C01031, https://doi.org/10.1029/2002JC001761.

——, ——, F. Feddersen, S. Elgar, and T. H. C. Herbers, 2005: Model-data comparisons of shear waves in the nearshore. *J. Geophys. Res.*, **110**, C05019, https://doi.org/10.1029/2004JC002541.

Oltman-Shay, J., P. A. Howd, and W. A. Birkemeier, 1989: Shear instabilities of the mean longshore current: 2. Field observations. *J. Geophys. Res.*, **94**, 18 031–18 042, https://doi.org/10.1029/JC094iC12p18031.

Özkan-Haller, H. T., and J. T. Kirby, 1999: Nonlinear evolution of shear instabilities of the longshore current: A comparison of observations and computations. *J. Geophys. Res.*, **104**, 25 953–25 984, https://doi.org/10.1029/1999JC900104.

Peregrine, D. H., 1998: Surf zone currents. *Theor. Comput. Fluid Dyn.*, **10**, 295–309, https://doi.org/10.1007/s001620050065.

Pezerat, M., X. Bertin, K. Martins, B. Mengual, and L. Hamm, 2021: Simulating storm waves in the nearshore area using spectral model: Current issues and a pragmatic solution. *Ocean Modell.*, **158**, 101737, https://doi.org/10.1016/j.ocemod.2020.101737.

Reniers, A. J. H. M., J. H. MacMahan, E. B. Thornton, and T. P. Stanton, 2006: Modelling infragravity motions on a rip-channel beach. *Coastal Eng.*, **53**, 209–222, https://doi.org/10.1016/j.coastaleng.2005.10.010.

——, ——, ——, and ——, 2007: Modeling of very low frequency motions during RIPEX. *J. Geophys. Res.*, **112**, C07013, https://doi.org/10.1029/2005JC003122.

Roelvink, D., A. Reniers, A. van Dongeren, J. van Thiel de Vries, R. McCall, and J. Lescinski, 2009: Modelling storm impacts on beaches, dunes and barrier islands. *Coastal Eng.*, **56**, 1133–1152, https://doi.org/10.1016/j.coastaleng.2009.08.006.

——, R. McCall, S. Mehvar, K. Nederhoff, and A. Dastgheib, 2018: Improving predictions of swash dynamics in XBeach:

The role of groupiness and incident-band runup. *Coastal Eng.*, **134**, 103–123, https://doi.org/10.1016/j.coastaleng.2017.07.004.

Scott, T., M. Austin, G. Masselink, and P. Russell, 2016: Dynamics of rip currents associated with groynes—Field measurements, modelling and implications for beach safety. *Coastal Eng.*, **107**, 53–69, https://doi.org/10.1016/j.coastaleng.2015.09.013.

Spydell, M., F. Feddersen, R. T. Guza, and W. E. Schmidt, 2007: Observing surf-zone dispersion with drifters. *J. Phys. Oceanogr.*, **37**, 2920–2939, https://doi.org/10.1175/2007JPO3580.1.

Valiente, N. G., G. Masselink, R. J. McCarroll, T. Scott, D. Conley, and E. King, 2020: Nearshore sediment pathways and potential sediment budgets in embayed settings over a multi-annual timescale. *Mar. Geol.*, **427**, 106270, https://doi.org/10.1016/j.margeo.2020.106270.